Dissertation presented to the Instituto Tecnológico de Aeronáutica, in partial fulfillment of the requirements for the degree of Master of Science in the Graduate Program of Physics, Field of Atomic Physics.

Victor Gabriel Morele Duarte

ELECTRONIC PROPERTIES OF TWISTED BILAYER GRAPHENE: PRESSURE AND ELECTROSTATIC BIAS DEPENDENCE

Dissertation approved in its final version by signatories below:

Prof. Dr. André Jorge Carvalho Chaves

Advisor

Prof[a]. Dr[a]. Lara Kühl Teles

Co-advisor

Prof[a]. Dr[a]. Emília Villani

Dean of Graduate Courses

Campo Montenegro
São José dos Campos, SP - Brazil
2023

Cataloging-in Publication Data
Documentation and Information Division

Morele Duarte, Victor Gabriel
Electronic properties of Twisted Bilayer Graphene: Pressure and electrostatic bias dependence / Victor Gabriel Morele Duarte.
São José dos Campos, 2023.
67f.

Dissertation of Master of Science – Course of Physics. Area of Atomic Physics – Instituto Tecnológico de Aeronáutica, 2023. Advisor: Prof. Dr. André Jorge Carvalho Chaves. Co-advisor: Prof[a]. Dr[a]. Lara Kühl Teles.

1. Grafeno. 2. Estruturas bidimensionais. 3. Semicondutores. 4. Propriedades ópticas. 5. Dispositivos optoeletrônicos. 6. Fotônica. 7. Optica. 8. Física. I. Instituto Tecnológico de Aeronáutica. II. Title.

BIBLIOGRAPHIC REFERENCE

MORELE DUARTE, Victor Gabriel. **Electronic properties of Twisted Bilayer Graphene: Pressure and electrostatic bias dependence**. 2023. 67f. Dissertation of Master of Science – Instituto Tecnológico de Aeronáutica, São José dos Campos.

CESSION OF RIGHTS

AUTHOR'S NAME: Victor Gabriel Morele Duarte
PUBLICATION TITLE: Electronic properties of Twisted Bilayer Graphene: Pressure and electrostatic bias dependence.
PUBLICATION KIND/YEAR: Dissertation / 2023

Victor Gabriel Morele Duarte
Avenida Andrômeda, 2531
12.230-000 – São José dos Campos–SP

ELECTRONIC PROPERTIES OF TWISTED BILAYER GRAPHENE: PRESSURE AND ELECTROSTATIC BIAS DEPENDENCE

Victor Gabriel Morele Duarte

Thesis Committee Composition:

Prof. Dr.	Manuel Malheiro	President	-	ITA
Prof. Dr.	André Jorge Carvalho Chaves	Advisor	-	ITA
Prof[a]. Dr[a].	Lara Kühl Teles	Co-advisor	-	ITA
Prof. Dr.	Luiz Fernando de Araújo Ferrão	Internal Member	-	ITA
Prof[a]. Dr[a].	Ingrid David Barcelos	External Member	-	CNPEM
Prof. Dr.	Diego Rabelo da Costa	External Member	-	UFC

ITA

To my family and friends.

Acknowledgments

Only 8.5 months have passed since I defended my undergraduate thesis, but it already feels like a distant memory. A lot has happened in my life since then, including some personal challenges and shortcomings. However, I managed to stay resilient and complete my master's work, finishing this dissertation in under 9 months after graduation, thanks to the support of several people.

Firstly, I want to thank my family for their unwavering support. My parents, Ronaldo and Danielly, have always been there for me with unconditional love and care. Their encouragement during these past few months played a significant role in helping me finish this degree. I am also grateful for my younger brothers, Danilo and Arthur, who bring joy to my life.

Next, I am thankful for my friends, especially Luiz and Gusthavo, who were great companions during this degree. We had thoughtful and productive conversations that enriched my academic journey. I also appreciate Lucas Taveira Caleiro for the collaborative work and discussions we had when I was starting to study the subjects that led to this master's dissertation. Last but not least, I am grateful for all the wonderful friends I made during this time, both within and outside of ITA. You all made my life happier.

I want to acknowledge the support and guidance of my advisor, Professor André, whose assistance was essential for the success of this work. He always went the extra mile to help me perform at my academic best, providing valuable advice and encouragement.

I am also thankful to all the professors from the GMSN research group for their dedication to teaching and fostering fundamental research at ITA, both at the undergraduate and graduate levels.

Finally, I extend my appreciation to CAPES, CNPq, and FAPESP for providing the financial support that allowed me to conduct this work and present it at scientific conferences.

"When life gets you down, you know what you gotta do? Just keep swimming." — Dory

Resumo

Este estudo investiga as interações luz-matéria em materiais 2D estratificados com *band gap* proeminente, focando na formação de éxcitons. O sistema específico sob exame consiste em duas camadas de grafeno com uma rotação, uma configuração bem documentada na literatura conhecida por sua manifestação de vários fenômenos exóticos. Ao contrário do grafeno em bicamada AB, este sistema não apresenta naturalmente um *band gap* em condições típicas, em contraste com a aplicação de um potencial elétrico.

Usando um modelo *tight-binding*, demonstramos teoricamente que a Bicamada Rotacionada de Grafeno (BRG) pode ser modulada através de um campo elétrico vertical e pressão para funcionar como um semicondutor de *gap* estreito, capaz de hospedar um espectro de éxcitons ligados anisotrópicos altamente hibridizados entre as camadas de grafeno. O *band gap* se abre sob alta pressão e pode ser aumentado pela inclusão do campo elétrico, alcançando valores de até 200 meV.

Em termos da estrutura de bandas, o *band gap* está localizado entre os pontos M e K da Zona de Brillouin da super-rede. Utilizando o formalismo das Equações Semicondutoras de Bloch (ESB), analisamos o impacto das interações elétron-elétron e observamos um aumento do *band gap*. Ao resolver as ESB homogêneas, demonstramos a presença de éxcitons altamente anisotrópicos com forte hibridização elétron-buraco entre diferentes camadas. Os espectros ópticos do sistema, que calculamos ao resolver as ESB completas, exibem uma ampla gama de picos de absorção, indicando que os éxcitons do GBR podem ser detectados experimentalmente por meio de assinaturas ópticas.

Abstract

This study investigates light-matter interactions in layered 2D materials with prominent band gaps, focusing on the formation of excitons. The specific system under examination consists of two layers of graphene with a twist, a well-documented configuration in the literature known for its manifestation of various exotic phenomena. Unlike AB bilayer graphene, this system does not naturally exhibit a band gap under typical conditions, in contrast to the application of an applied bias.

Using a tight-binding model, we theoretically demonstrated that Twisted Bilayer Graphene (TBG) can be modulated through vertical bias and pressure to function as a narrow band gap semiconductor, capable of hosting a spectrum of anisotropic bound excitons highly hybridized between the graphene layers. The gap opens under high pressure and can be further enhanced by an electric bias, with values reaching up to 200 meV.

In terms of the band structure, the band gap is located between the M and K points of the superlattice Brillouin Zone. Utilizing the Semiconductor Bloch Equations (SBE) formalism, we analyze the impact of electron-electron interactions and observe an enhancement of the band gap. By solving the homogeneous SBE, we demonstrate the presence of highly anisotropic excitons with strong electron-hole hybridization between different layers. The optical spectra of the system, which we calculated by solving the complete SBE, exhibit a diverse range of absorption peaks, which indicate that the excitons of TBG can be detected experimentally by optical signatures.

List of Figures

Contents

1 Introduction

1.1 Brief introduction to 2D materials and exciton formation

Atomically thin materials have attracted the attention of a myriad of both theoretical and experimental works in the recent years in the field of Condensed Matter Physics. These materials, commonly called two-dimensional (2D), are strongly susceptible to the neighboring environment, which makes them highly tunable by external parameters of easy control in a laboratory setting, such as electromagnetic fields, temperature, pressure, vacancies, impurities and strain. Some usual examples of such materials are graphene, 2D transition metal dichalcogenides (TMD) (MANZELI *et al.*, 2017), hexagonal boron nitride (hBN) (ZHANG *et al.*, 2017) and black phosphorus (LING *et al.*, 2015).

Graphene is the first isolated 2D material and came as a shock to the community due to its extraordinary mechanical and electronic properties (GEIM, 2009). It is formed by a planar sheet of carbon atoms displaced in a triangular lattice forming hexagons. It is a semi-metal, whose physics is severely determined by the formation of Dirac cones in its band structure, with zero band gap. hBN can be seen as a close brother of graphene, with an identical structure except for the sublattice symmetry break due to different atomic species. This symmetry break induces a high bandgap opening, which makes this material an insulator (ZHANG *et al.*, 2017).

2D TMDs, on the other hand, also have a similar atomic structure, but only when looking from the top. They have the chemical formula MX_2, where M is the metal (usually Mo or W) and X is the chalcogen (usually S or Se). Despite its non-trivial three-dimensional structure, it is also formed by a triangular lattice, and forms hexagons when observed from the top. 2D TMDs are usually semiconductors due to their middle-range band gaps (MANZELI *et al.*, 2017). For this reason, when light is shined in such materials, electrons can be excited from valence to conduction bands, forming an excited state (DAVYDOV, 1964). This excited electron leaves an unoccupied state behind, with an effectively positive charge, which is called a hole. The hole couples with the electron

via a Coulomb interaction, forming a bound state named as exciton, that reduces the total energy of the material (DAVYDOV, 1964). Excitons are elementary quasi-particle excitations that transport energy without net charge transfer. They describe the most fundamental interactions between light and matter, and are of extreme importance to the description of the low-energy physics of crystalline materials. Speaking in terms of ideal materials, it is essential that a material has a bandgap in order to form excitons. So, ideally, regular graphene or metallic materials cannot host excitons, for instance, but any semiconductor or insulator potentially can in general.

2D materials can also be stacked to form heterostructures with novel electronic and optical properties not intrinsic to the parent materials nor to common bulk materials (GEIM; GRIGORIEVA, 2013), which gives room to a plethora of possibilities with a wide range of degrees of freedom only limited by human creativity. As we will discuss in subsequent sections, previous works have shown how the behavior of heterostructures can be severely affected by external effects, specially by twisting its layers.

1.2 The magic of twist in graphene and the rise of twistronics

It has long been known that material properties depend on the way they are stacked. In the case of bilayer graphene, the electronic structure is quite different in the AA and AB stacking configurations (GEIM, 2009). In the AB configuration, the band structure of graphene around the top of the valence band and bottom of the conduction band are two parabolas with a zero bandgap that can be controlled by a perpendicular electric field (CASTRO *et al.*, 2010), while the AA configuration is essentially the same as graphene but with a higher degeneracy. Experiments on Twisted Bilayer Graphene (TBG) began in 2010 when Eva Andrey's group observed the presence of Van Hove singularities (LI *et al.*, 2010), which could already be theoretically predicted using a continuum model developed in 2007. In 2010, the presence of flat bands at rotation angles between 1.6° and 1.3° was also predicted (MORELL *et al.*, 2010), and a continuum model that reached the same conclusion appeared the following year (BISTRITZER; MACDONALD, 2011). Interest in twisted layered 2D materials has been revamped since the publication of experiments conducted by Jarillo-Herrero's group showing superconductive behavior in bilayer graphene twisted by 1.1° (CAO *et al.*, 2018). This angle became known as the magic angle of TBG in the related literature. As Ref. (CAO *et al.*, 2018) shows, the electronic bands of TBG near the Fermi level form a pair of doubly degenerate Dirac cones, which we were able to reproduce in previous work using a tight-binding model (DUARTE, 2022).

The kinetic energy of electronic excitations in flat bands is essentially zero. Therefore,

the system is dominated by interactions, and the electrons are strongly correlated. Superconductive TBG has motivated a series of experiments in graphene and similar systems, showing a plethora of intriguing physical phenomena (CAO *et al.*, 2016; SONG *et al.*, 2019; PARK *et al.*, 2019; POLSHYN *et al.*, 2019; KERELSKY *et al.*, 2019; XIE; MACDONALD, 2020; CEA; GUINEA, 2020; CAO *et al.*, 2020; CHOI *et al.*, 2021).

On the other hand, a rotation between two layers of two-dimensional materials occurs naturally in heterostructures when the constituents have different lattice parameters, forming Moiré patterns. Before exploring heterostructures, we will discuss the formation of excitons in TMDs.

1.3 TMD's bilayers: State-of-the-art

2D TMDs exhibit strong spin-orbit interaction, which breaks spin degeneracy in the conduction band (MANZELI *et al.*, 2017). They present a direct band-gap located at the **K** point, and much weaker electron-electron interactions compared to their 3D counterparts. For this reason, the electrostatic attraction between electrons and holes is stronger, resulting in larger binding energies. Selection rules allow excitons to be classified as "bright" or "dark", depending on whether they couple with photons or not. Bright excitons appear as intense peaks in absorption or photoluminescence experiments. Dark excitons, on the other hand, have been proposed for use as qubits (MARAGKOU, 2015). The position of dark excitons can be tuned by the electrostatic environment, doping, and temperature. In this section, we discuss heterostructures of 2D TMDs before delving into excitons.

Ref. (AL., 2019) explored the effect of rotation between layers of $MoSe_2$ and WS_2 on the hybridization of chalcogen orbitals between layers. In a theoretical investigation based on Density Functional Theory (DFT) calculations, Ref. (NAIK; JAIN, 2018) explored 2H stacked bilayers of MX_2, where M = Mo or W and X = S, twisted by 3.5° (AA stacking, $B^{S/Mo}$, and $B^{Mo/S}$) and 56.5° (AB stacking, $B^{S/S}$, and $B^{Mo/Mo}$), forming flat bands at the top valence band region. As a result, they classified these morphologies as "magic angles" of the studied species.

The study of the properties of layered 2D TMDs dates back to the early 1960s (AL., 2013). The great interest in this type of study is justified by drastic behavior changes observed when stacking two layers of 2D TMDs, such as transitions from indirect to direct band gap (AL., 2017). Among the first experimental works reporting the modulation of the twist angle between layers as a degree of freedom in homo- and heterobilayers of 2D TMDs, the investigation conducted by Ref. (ZANDE; AL., 2014) stands out, where bilayers of CVD-synthesized MoS_2 were studied. They established that S···S repulsions between layers varies with the twist angle, and are responsible for modulating the electronic structure of

the material.

Ref. (HUANG, 2014) found that the twist between layers of MoS_2 is responsible for maxima and minima in the photoluminescence intensity ratio, with maxima at 0° and 60° and minima at 30° and 90°. This study also reported DFT calculations for the studied systems, confirming the change in the interaction energy between MoS_2 layers tuned by twist. On the other hand, Ref. (KANG; AL., 2013) pioneered the study of MoS_2-$MoSe_2$ heterobilayers twisted by 2° using a supercell of 6630 atoms. This study showed that the modulation by twist of S···Se interactions between layers have a great influence on the valence band profile of the material, which is quite localized, but exerts little influence on the conduction band minimum.

On the other hand, theoretical studies exploring 2D TMD bilayers twisted by less than 3.5° can become challenging due to the formation of supercells with large numbers of atoms. This motivated Ref. (NAIK *et al.*, 2019) to propose a combination of the Stillinger-Weber (SW) force field, to describe the intra-layer interactions, with the Kolmogorov-Crespi (KC) potential, to describe the inter-layer interactions, for relaxation calculations of MX_2, where M = Mo or W and X = S or Se, in their homo- and hetero-bilayers. The results of the relaxations performed using the SW-KC combination were comparable to experimental parameters obtained from DFT calculations employing the LDA functional with van der Waals corrections (vdW-DF-C09).

The breaking of certain symmetries, such as the mirror symmetry of 2D TMD monolayers, plays a fundamental role in determining the electronic properties of the material. For this reason, the synthesis of Janus TMD monolayers is crucial for the development of new materials based on 2D TMDs. The first experimental results reporting the synthesis of Janus monolayers dates back to 2017. Ref. (LU; AL., 2017) reported the synthesis of a MoSSe monolayer from a triangular nanoflake of MoS_2 synthesized by CVD on sapphire. One of the S layers was exfoliated and replaced with a layer of Se, resulting in the final material. Ref. (ZHANG; AL., 2017) reported the synthesis of MoSSe in multilayers starting from multilayers of $MoSe_2$ and revealed that sulfur (S) at 800°C can induce the sequence S−Mo−Se–Se−Mo−Se in the final product. Ref. (YIN *et al.*, 2018) explored the energetic properties of MoSSe using DFT/ Perdew-Burke-Ernzerhof (PBE) calculations, varying the number of layers from 1 to 3. This investigation determined that the energetically most stable bilayer MoSSe has an AC stacking, and that the variation of stacking modes of Janus bilayers can modulate the bandgap of the material within the range of 0.81 eV to 1.45 eV in the infrared and visible spectrum regions.

In parallel, Ref. (LI *et al.*, 2017) reported theoretical results for vertically stacked MoSSe−WSSe bilayers, outlining that quasiparticle corrections significantly modify the band structure of the studied materials, and excitonic effects play a dominant role in the optical response. Additionally, vertically stacked bilayers of MoSSe−WSSe exhibit charge

transfer effects between layers and type-II band alignment, which is desirable for energy conversion materials.

The theoretical study conducted by Ref. (LONG *et al.*, 2019) explores MoSSe bilayers with Se–Mo–S···Se–Mo–Se interactions and relative rotations between the monolayers of 13.17° and 21.79°. They found that the difference in electronegativity between S and Se induces an intrinsic electric field, responsible for the type-II band alignment. The contributions of the valence band maximum and conduction band minimum derive from individual contributions between the monolayers that form the system. Moreover, changing the twist does not modify the observed band alignment for the non-rotated case. However, variations in twist can affect the flatness of the band near the Γ point, which determines the valence band maximum in the indirect bandgap.

Modifications in the polytype of monolayers can also induce distinct behaviors in 2D TMD monolayers, motivating experimental studies aimed at modifying the synthesized monolayer polytypes. The theoretical study of Ref. (ER *et al.*, 2018) reports the results for Janus monolayers formed by possible combinations of MXY, with M = Mo or W and X, Y = S, Se or Te, for the 2H and 1T′ polytypes. They demonstrated that the charge imbalance between atoms X and Y breaks the out-of-plane symmetry of the monolayer, and the octahedral distortion brings the energies of the d_{z^2} orbitals closer to the Fermi level.

Ref. (KRETSCHMER *et al.*, 2017) also outlines the approximation of the d_{z^2} orbital to the metallic behavior of the 1T′/2H polymorphic morphology of MoS_2. This morphology was synthesized by Ref. (LIN, 2018), who detailed the collective movements of chalcogen planes responsible for the polytype change in monolayer domains through transmission electron microscopy studies. However, there are no studies investigating polymorphs in bilayers and the reciprocal effects between polymorphism and layer rotation angle in homo- or hetero-bilayers of 2D TMDs, and how these parameter and morphology changes affect the electronic structure of the systems. Such studies are essential due to the loss of symmetries within and out of the plane of the material layers.

The advancement in the field of 2D TMD studies has primarily focused on compounds that include transition metals from group 6, with MoS_2 being the most popularly studied 2D TMD. However, detailed studies of TMDs from other regions of the periodic table have revealed interesting properties. For example, group 10 TMDs exhibit semiconductor-to-metal transitions under strain and varying numbers of layers, as well as topological surface states (MANZELI *et al.*, 2017). Among the group 10 2D TMDs, PtS_2 stands out. It was first synthesized in its bilayer form by Ref. (ZHAO *et al.*, 2019), who observed the strong covalent nature of the intralayer S···S interactions in the material, leading to a reduced band gap.

As described by Ref. (ZHAO *et al.*, 2019) through experimental and theoretical studies, the strong hybridization between chalcogens from different layers is responsible for the anticipated high electronic mobility of PtS_2 compared to its group 6 counterparts. Literature works clearly describe how the electronic properties of PtS_2 change with the number of layers. In a recent study, (DENG *et al.*, 2019) evaluated PtS_2/MoS_2 bilayers with different twists, considering strain effects on the material. They observed that a 30 twist led to a peak in absorption, and changes in twist modulated the material's band gap. They also observed charge transfer from PtS_2 to MoS_2.

Indeed, it is worth noting that only recently a Janus form of PtS_2, namely PtSSe, was investigated by Ref. (PENG *et al.*, 2019), highlighting the lack of systematic studies on Janus forms of this TMD in bilayers. Among the group 10 2D TMDs, $PdSe_2$ also stands out. It has been synthesized in a controlled manner by Refs. (ZENG *et al.*, 2018; LI *et al.*, 2018), exhibiting a pentagonal polymorph, which is distinct from the polymorphs associated with group 6 2D TMDs and the 1T phase of PtS_2. However, there are no theoretical studies investigating the effects of twist in homo- or heterobilayers of $PdSe_2$, which opens up opportunities for further investigations exploring this TMD in this context.

Chemical composition modifications, such as in Janus monolayers, and polymorphic changes, as in the case of different polymorphs, lead to stress effects in the systems due to the presence of regions with different atomic radii and lattice parameters. These effects modify the orbital overlaps and, consequently, the electronic structure of the bilayer. However, different levels of hybridization can also be achieved in materials whose layers preserve symmetries within and between layers by applying stress to the material. Ref. (BHATTACHARYYA; SINGH, 2012) investigated homobilayers of MoX_2, where X = S, Se or Te, and WY_2, where Y = S or Se, under compressive normal stress up to 20 GPa, with the studied bilayers exhibiting AA and AB stackings.

Indeed, it has been observed that all TMDs' bilayers undergo a transition from semimetal to metal with the application of stress, which differs from the behavior obtained for monolayers. The modulation of the material's band gap has also been observed, and it can be explained by the increased contribution of the chalcogen's d orbitals to the conduction band minimum and the decrease in the contributions from the metal's d orbitals and the chalcogen's p orbitals as compressive normal stress is applied to the system.

Ref. (SHARMA *et al.*, 2014) also observed semiconductor-to-metal transitions with the application of tensile stress in heterobilayers of MoX_2 and WX_2, where X = S or Se. They also observed changes in the effective electron mass through theoretical studies. Ref. (DONG *et al.*, 2017) reported in a theoretical study that Janus homobilayers of previously synthesized materials, such as MoSSe, in all stacking sequences without angle rotation between the layers exhibit charge polarizations facilitated by compressive stresses applied in- and out-of- monolayers' planes. The observed results in this study can also

be attributed to the differences in electronegativity between the chalcogen species being investigated.

1.4 Twisted TMDs: Moiré Potential

When we stack two layers of TMDs, we can have both intralayer excitons, where the electron and hole are located in the same layer, and interlayer excitons, where the electron and hole reside in different layers. In fact, we can observe even an intermediate situation, where the excitons are hybridized between the layers (LUCATTO *et al.*, 2019). When the layers are rotated with respect to each other, as naturally occurs in heterostructures, a superlattice is formed, giving rise to excitons trapped in the Moiré potential, denominated as Moiré excitons.

These Moiré excitons in TMDs possess large binding energies (>100 meV) and can exist in either interlayer or intralayer configurations. Their optical activity depends on the angular momentum and total momentum. Recently, these systems have emerged as an interesting platform for achieving strong nonlinear effects in quantum optics and studying interacting exciton states in confined potentials. Furthermore, the behavior of excitons with rotational alignment, forming a Moiré pattern, is a topic of great current interest due to its rich physics to be explored (SHIMAZAKI *et al.*, 2020; BAI *et al.*, 2020; LI *et al.*, 2020; ROSENBERGER *et al.*, 2020; MERKL *et al.*, 2020; HALBERTAL *et al.*, 2021; ANDERSEN *et al.*, 2021; TANG *et al.*, 2021; XU *et al.*, 2021; BREM *et al.*, 2020; BAEK *et al.*, 2020; ZHANG *et al.*, 2020; SHABANI *et al.*, 2021; CHOI *et al.*, 2020; ERKENSTEN *et al.*, 2021; FÖRG *et al.*, 2021).

1.5 Objectives of this work

In the current chapter, we have demonstrated the rich physics and strong technological potential of layered twisted 2D materials. Moreover, since we know that bilayer graphene can be gapped through the application of a bias (NETO *et al.*, 2009) and that 2D materials can host excitons with strong binding energies, we decided to investigate the presence of excitons in TBG. The insertion of a twist came as an additional element since the more common stackings of graphene were well studied theoretically already, and twisting the layers of heterostructures can give rise to lots of interesting physical phenomena, as we discussed. In this work, we explore the interplay of rotation, electric field, and pressure in the electronic and optical properties of bilayer graphene. It builds upon prior research, starting as an undergraduate research internship and progressing into an undergraduate thesis (DUARTE, 2022), culminating in this masters dissertation.

First, we model the atomic structure of TBG in the context of single-particle quantum mechanics, showing how the lattice modulates the behavior of the electrons via the tight-binding approximation (MARDER, 2010). Next, to study how this system screens its own electronic interactions, we use a formalism adapted from the works of Adler (ADLER, 1962) and Wiser (WISER, 1963) to layered 2D materials. Through this approach, we derive a dielectric function, that describes electronic screening for any external potential. Finally, to study exciton formation, we move up to many-particle physics in order to derive the Semiconductor Bloch Equations (SBE) tailored to TBG, which will allow us to study the excitonic spectrum and light interactions via optical properties, such as the absorption spectrum (CHAVES, 2018; KIRA; KOCH, 2011).

2 Tight-binding model

2.1 Atomic structure

Here we will model TBG as two planar graphene layers, *i.e.*, buckling effects are neglected. We choose a coordinate system in which the layers are located at $z = 0$ and $z = d$, such that d is the vertical distance between the layers. The unit vectors that form the standard basis of 3D space are denoted as $\mathbf{e}_i$, $i = x, y, z$. Each graphene lattice is composed of two triangular sublattices A and B, and their crystalline orientations are rotated relative to each other by an angle θ. Fig. 2.1 shows the TBG lattice from the reference point of an observer looking from above, in the direction $-\mathbf{e}_z$. The sublattice

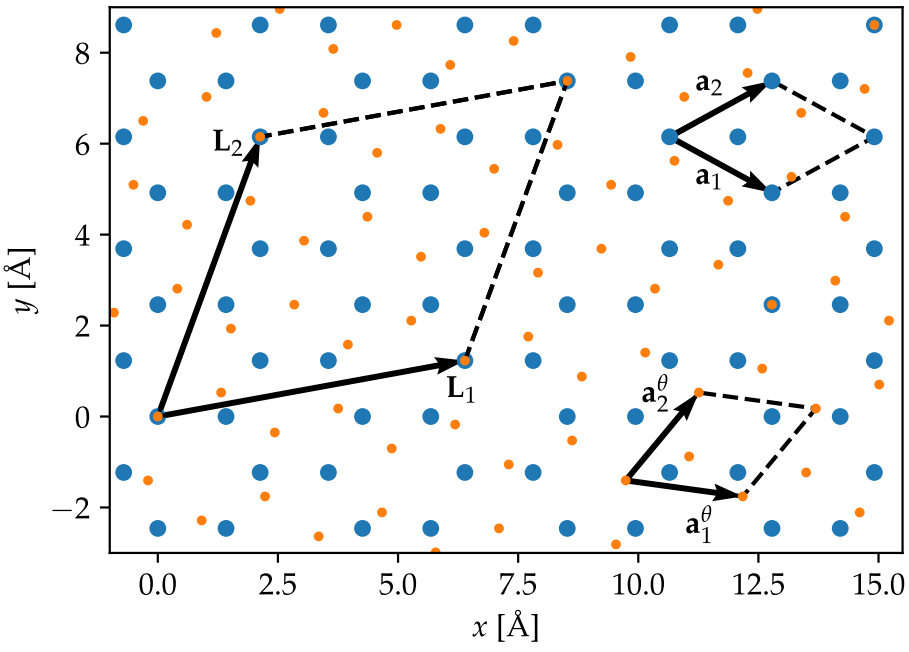

FIGURE 2.1 – (Color online) Schematic representation in real space of TBG for $\theta(1, 1) \approx 21.8°$ looking from above. The unrotated layer ($\ell = 1$) is presented in blue bigger dots, and the rotated one ($\ell = 2$), in orange smaller dots for clarity. The selected unit cell is highlighted using the primitive vectors $\mathbf{L}_1$, $\mathbf{L}_2$ and black dashed lines. The primitive vectors and unit cells of each individual layer of graphene are also shown.

vectors can be explicitly written as

$$\mathbf{r}_{A1} = m\mathbf{a}_1 + n\mathbf{a}_2, \tag{2.1a}$$

$$\mathbf{r}_{B1} = \mathbf{r}_{A1} + (\mathbf{a}_1 + \mathbf{a}_2)/3, \tag{2.1b}$$

$$\mathbf{r}_{A2} = \mathrm{rot}(\theta)\mathbf{r}_{A1} + d\mathbf{e}_z, \tag{2.1c}$$

$$\mathbf{r}_{B2} = \mathrm{rot}(\theta)\mathbf{r}_{B1} + d\mathbf{e}_z, \tag{2.1d}$$

where $m, n \in \mathbb{Z}$, $\mathbf{a}_{1,2} = a(\sqrt{3}\mathbf{e}_x \pm \mathbf{e}_y)/2$ are the primitive vectors of graphene, $a = 2.46$ Å is a lattice constant, and $\mathrm{rot}(\theta)$ is the rotation matrix

$$\mathrm{rot}(\theta) = \begin{bmatrix} \cos\theta & -\sin\theta & 0 \\ \sin\theta & \cos\theta & 0 \\ 0 & 0 & 1 \end{bmatrix}. \tag{2.2}$$

The formalism developed in this section will be restricted to TBG structures with a well defined superlattice and unit cell. In other words, the TBG superlattice must be periodic. This is guaranteed if some atomic positions of different layers match horizontally, which can be written mathematically as

$$m_1\mathbf{a}_1 + n_1\mathbf{a}_2 = m_2\mathbf{a}_1 + n_2\mathbf{a}_2 \tag{2.3}$$

for some sets of integers $\{m_1, n_1, m_2, n_2\}$. This Diophantine equation is known in the related literature as the commensurate condition (SANTOS *et al.*, 2007; MELE, 2010; SHALLCROSS *et al.*, 2010; SANTOS *et al.*, 2012). Its solutions are given in terms of an arbitrary pair of co-prime positive integers p, q, such that the possible twist angles between graphene layers are

$$\theta(p, q) = \arccos\left(\frac{3p^2 + 3pq + q^2/2}{3p^2 + 3pq + q^2}\right). \tag{2.4}$$

The primitive vectors of the resulting superlattices are

$$\mathbf{L}_1 = \begin{cases} \left(p + \dfrac{q}{3}\right)\mathbf{a}_1 + \dfrac{q}{3}\mathbf{a}_2, & \text{if q is disivible by 3,} \\ p\mathbf{a}_1 + (p+q)\mathbf{a}_2, & \text{otherwise,} \end{cases} \tag{2.5}$$

$$\mathbf{L}_2 = \mathrm{rot}(60^\circ)\mathbf{L}_1. \tag{2.6}$$

For subsequent discussions, we will denote by $\mathbf{R} = m\mathbf{L}_1 + n\mathbf{L}_2$ $(m, n \in \mathbb{Z})$ the superlattice vectors and by $\boldsymbol{\delta}_\ell$ the subset of basis vectors of the graphene layer $\ell = 1, 2$ that define the unit cell of the superlattice, as illustrated in Fig. 2.1. Mathematically, $\boldsymbol{\delta}_\ell$ is

any lattice vector whose projection in the xy plane can be written as

$$x\mathbf{L}_1 + y\mathbf{L}_2,\ 0 \leq x, y < 1. \tag{2.7}$$

Any sublattice vector (2.1) can be rewritten generically as $\mathbf{R}+\boldsymbol{\delta}_\ell$. The compact notations $\sum_\ell = \sum_{\ell=1}^{2}$, $\sum_{\mathbf{R}}$ and $\sum_{\boldsymbol{\delta}_\ell}$ will be used to indicate sums over all layers, superlattice vectors and basis vectors, respectively.

2.2 Tight-binding Hamiltonian

We make use of the tight-binding approximation to describe the Hamiltonian of TBG, through the second quantization formalism. More information regarding this choice can be found on Ref. (DUARTE, 2022). In a small range near the highest energy level occupied by electrons of TBG in the ground state (namely, the Fermi level), chemical intuition, as well as Density Functional Theory calculations (POLINI *et al.*, 2008), tells us that the p_z orbitals are energetically dominant. This energy scale is commonly referred as low energy physics in the literature, since it contains the electronic states more easily accessible in experiments through external perturbations and will give us the insight about electronic and optical properties we are interested in. Thus, our model will be restricted to the electrons with states described by p_z orbitals, denominated p_z electrons for short.

Moreover, we need to introduce the creation and annihilation operators of p_z electrons, written generically in the forms $\psi_i^\dagger$ and ψ_i, respectively. The operator $\psi_i^\dagger$ creates an electron with a state described by the index (or set of indices) i. The conjugate operator ψ_i, on the other hand, annihilates that same electron. We also introduce the vacuum state $|0\rangle$, *i.e.*, the ground state where all the electrons occupy the lowest possible energy states, respecting the Fermi exclusion principle. In this manner, all the electronic states up to the Fermi level are occupied. Here we introduce the Fermi energy E_F, defined as the energy of the Fermi level. Since electrons are fermionic particles, the anti-commutator relation

$$\{\psi_i, \psi_j^\dagger\} = \delta_{ij} \tag{2.8}$$

must be satisfied.

The tight-binding Hamiltonian in its simplest form becomes

$$\mathcal{H}_{\text{TB}} = \sum_{\ell\ell'} \sum_{\boldsymbol{\delta}_\ell \boldsymbol{\delta}_{\ell'}} \sum_{\mathbf{R}\mathbf{R}'} t(\mathbf{R} + \boldsymbol{\delta}_\ell - \mathbf{R}' - \boldsymbol{\delta}'_{\ell'}) c^\dagger_{\mathbf{R}+\boldsymbol{\delta}_\ell} c_{\mathbf{R}'+\boldsymbol{\delta}_{\ell'}}, \tag{2.9}$$

where $t(\mathbf{r})$ is the transfer integral (SLATER; KOSTER, 1954; MOON; KOSHINO, 2013) and $c^\dagger_{\mathbf{r}}$ is the fermionic operator that creates a p_z electron centered at $\mathbf{r}$. By assuring commen-

surability (see Sec. 2.1), the atomic structure of TBG is guaranteed to be periodic. To take advantage of this periodicity, we Fourier transform the operators $c^\dagger_{\mathbf{r}}$ using

$$c^\dagger_{\mathbf{R}+\boldsymbol{\delta}_\ell} = \frac{1}{\sqrt{N}} \sum_{\mathbf{k}}^{\mathrm{BZ}} e^{\mathrm{i}\mathbf{k}\cdot(\mathbf{R}+\boldsymbol{\delta}_\ell)} b^\dagger_{\mathbf{k}\boldsymbol{\delta}_\ell}, \tag{2.10}$$

where N is the number of unit cells of the material and $\sum_{\mathbf{k}}^{\mathrm{BZ}}$ is a sum over wavevectors restricted to the first Brillouin Zone (BZ) of the material. The inverse relation

$$b^\dagger_{\mathbf{k}\boldsymbol{\delta}_\ell} = \frac{1}{\sqrt{N}} \sum_{\mathbf{R}} e^{-\mathrm{i}\mathbf{k}\cdot(\mathbf{R}+\boldsymbol{\delta}_\ell)} c^\dagger_{\mathbf{R}+\boldsymbol{\delta}_\ell} \tag{2.11}$$

is guaranteed by the orthogonality of the Fourier basis

$$\sum_{\mathbf{R}} e^{\mathrm{i}\mathbf{k}\cdot\mathbf{R}} = N\delta_{\mathbf{k}\mathbf{0}}, \tag{2.12}$$

for $\mathbf{k}$ restricted to the BZ. Using the Fourier transform (2.10) and the orthogonality relation (2.12), we rewrite the Hamiltonian (2.9) in momentum space as

$$\mathcal{H}_{\mathrm{TB}} = \sum_{\mathbf{k}}^{\mathrm{BZ}} \sum_{\ell\ell'} \sum_{\boldsymbol{\delta}_\ell \boldsymbol{\delta}_{\ell'}} \sum_{\mathbf{R}} e^{\mathrm{i}\mathbf{k}\cdot(\mathbf{R}+\boldsymbol{\delta}_\ell-\boldsymbol{\delta}_{\ell'})} t(\mathbf{R}+\boldsymbol{\delta}_\ell-\boldsymbol{\delta}_{\ell'}) b^\dagger_{\mathbf{k}\boldsymbol{\delta}_\ell} b_{\mathbf{k}\boldsymbol{\delta}_{\ell'}}, \tag{2.13}$$

where $\mathbf{k}$ is the Bloch wavevector and $b^\dagger_{\mathbf{k}\boldsymbol{\delta}_\ell}$ is the transformed basis, indexed by the finite set of vectors $\boldsymbol{\delta}_\ell$.

We emphasize the importance of deriving a formulation for the Hamiltonian in a finite basis. This allows us to numerically construct and diagonalize Hamiltonian matrices. Here, we used the finite set of vectors $\boldsymbol{\delta}_\ell$ to label this basis, taking the periodicity of the infinite system into account. As will be shown later, the transfer integrals are position-dependent functions that decay exponentially with distance. Thus, the infinite sum over lattice vectors $\sum_{\mathbf{R}}$ in Eq. (2.13) can be safely truncated.

The basis also depends on the wavevector $\mathbf{k}$, but the Hamiltonian is diagonal in that index since there is no coupling between pairs of different wavevectors. In a sense, one can think of Eq. (2.13) as a block diagonal matrix with respect to the index $\mathbf{k}$. Since the eigenvalues of a block diagonal matrix are exactly equal to the eigenvalues of each separate block, each block can be diagonalized independently. Physically, this means we can calculate the eigenenergies separately for each value of $\mathbf{k}$, and the complete spectrum of eigenenergies as a function of $\mathbf{k}$ forms the electronic band structure of the crystal in 3D space, denominated simply as band structure in subsequent discussions for short. In later sections, we will derive the complete form of the Hamiltonian we need to diagonalize, as a function of a set of parameters, and explain further the nature of the diagonalization

process.

2.3 Transfer integral

In the tight-binding picture, the transfer integral $t(\mathbf{r})$ describes the energy parameters associated with hoppings of electrons between different sites. In the particular case of TBG, all sites are single p_z orbitals. Since they do not all align vertically due to the presence of two stacked graphene layers, geometric aspects of the p_z orbital distribution in space must be taken into consideration. We closely follow the clever procedure used by Ref. (MIRZAKHANI *et al.*, 2020) to handle this problem by considering that any interaction between pairs of p_z orbitals can be decomposed into pure π- and σ-like bonds, as will be discussed in the following.

If $\mathbf{r}$ is the distance vector between two p_z orbitals, then $\cos\theta_{pp} = (\mathbf{r}\cdot\mathbf{e}_z)/r$ is the cosine of the angle that $\mathbf{r}$ forms with the z axis, as shown in Fig. 2.2. Each p_z orbital

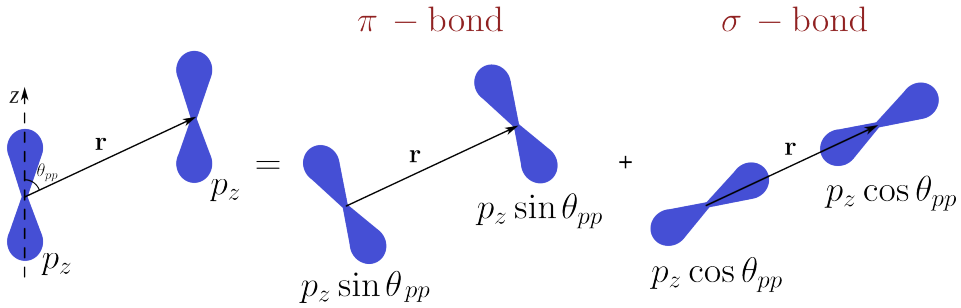

FIGURE 2.2 – (Color online) Interaction between a pair of p_z orbitals, decomposed into π- and σ-like interactions. The lobes are projected onto a pair of axis, one parallel and one perpendicular to the vector $\mathbf{r}$ connecting the orbital centers.

can be decomposed into a $p_z \cos\theta_{pp}$ in the direction parallel to $\mathbf{r}$, and a $p_z \sin\theta_{pp}$ in the orthogonal direction. The $p_z \cos\theta_{pp}$-$p_z \cos\theta_{pp}$ interaction resembles a σ-bond, and the $p_z \sin\theta_{pp}$-$p_z \sin\theta_{pp}$ one, a π-bond. Orthogonal interactions $p_z \cos\theta_{pp}$-$p_z \sin\theta_{pp}$ vanish due to the opposite signs of the p_z orbital globes. Denoting the pure σ- and π-like transfer integrals by $V_{pp\sigma}(r)$ and $V_{pp\pi}(r)$, we can write

$$t(\mathbf{r}) = V_{pp\sigma}(r)\cos^2\theta_{pp} + V_{pp\pi}(r)\sin^2\theta_{pp}. \tag{2.14}$$

The final step to express $t(\mathbf{r})$ in the same way as Ref. (MIRZAKHANI *et al.*, 2020) is to apply $\cos\theta_{pp} = (\mathbf{r}\cdot\mathbf{e}_z)/r$ and $\sin^2\theta_{pp} = 1 - \cos^2\theta_{pp}$:

$$t(\mathbf{r}) = V_{pp\sigma}(r)\left(\frac{\mathbf{r}\cdot\mathbf{e}_z}{r}\right)^2 + V_{pp\pi}(r)\left[1 - \left(\frac{\mathbf{r}\cdot\mathbf{e}_z}{r}\right)^2\right]. \tag{2.15}$$

Atomic orbitals have exponentially decaying tails far from their centers. For this

reason, the pure σ and π transfer integrals are also assumed to decay exponentially. Thus, they are modelled as exponential functions with fitting parameters chosen to reflect physical properties of the real system. First, the hoppings of the nearest neighbors in the same layer (intralayer):

$$V_{pp\pi}(a_{cc}) = V^0_{pp\pi} \approx -2.7\,\mathrm{eV}, \tag{2.16}$$

and between different layers (interlayer):

$$V_{pp\sigma}(d_0) = V^0_{pp\sigma} \approx 0.48\,\mathrm{eV}. \tag{2.17}$$

This values are set in agreement with the band structures of monolayer graphene and AB bilayer graphene, respectively. The constant $a_{cc} = a/\sqrt{3} \approx 1.42$ Å is the carbon-carbon bond length, and $d_0 \approx 3.35$ Å, the distance d between graphene layers at equilibrium. Second, the decay rate

$$\frac{1}{\delta_0} = -\frac{\dot{V}_{pp\sigma}(r)}{V_{pp\sigma}(r)} = -\frac{\dot{V}_{pp\pi}(r)}{V_{pp\pi}(r)}, \tag{2.18}$$

expressed in terms of the decay length $\delta_0 = 0.148a$, where $(\dot{})$ denotes a derivative with respect to r. Under all these considerations, the pure transfer integrals are fitted as

$$V_{pp\pi}(r) = V^0_{pp\pi} \exp\left(-\frac{r - a_{cc}}{\delta_0}\right), \tag{2.19}$$

$$V_{pp\sigma}(r) = V^0_{pp\sigma} \exp\left(-\frac{r - d_0}{\delta_0}\right). \tag{2.20}$$

We emphasize that, for pragmatic reasons, the transfer integral must be truncated to a portion of near enough neighbors in order to truncate the infinite $\sum_{\mathbf{R}}$ sums of Eq. (2.13) to finite sums. This is well justified since the transfer integral decay exponentially as discussed previously. In this work, the intralayer hoppings are restricted to first nearest neighbors, *i.e.*, hoppings between carbon atoms distant by a_{cc}. The interlayer hoppings, on the other hand, are restricted to hoppings between carbon atoms distant by $4a_{cc}$ at most. In other words, the transfer integral for interlayer hoppings is only evaluated for $r < 4a_{cc}$.

2.4 First order (classical) electric-field effect

By applying a uniform electric field $\boldsymbol{\mathcal{E}} = \mathcal{E}\mathbf{e}_z$ to TBG, a vertical electric potential $v(z) = v(0) - \mathcal{E}z$ is induced. We set the reference $v(d/2) = 0$, such that the potentials at the graphene layers are $v(0) = \mathcal{E}d/2$ and $v(d) = -\mathcal{E}d/2$. In agreement with Ref. (NETO *et al.*, 2009), we include the first-order (classical) effect of an electric field perpendicular

to the graphene sheets by adding the diagonal term

$$\mathcal{H}_V = \frac{V}{2}\sum_{\mathbf{R}}\sum_{\ell\boldsymbol{\delta}_\ell} s_\ell c^\dagger_{\mathbf{R}+\boldsymbol{\delta}_\ell} c_{\mathbf{R}+\boldsymbol{\delta}_\ell} = \frac{V}{2}\sum_{\mathbf{k}}^{\mathrm{BZ}}\sum_{\ell\boldsymbol{\delta}_\ell} s_\ell b^\dagger_{\mathbf{k}\boldsymbol{\delta}_\ell} b_{\mathbf{k}\boldsymbol{\delta}_\ell} \tag{2.21}$$

to the Hamiltonian, where $s_\ell = \delta_{\ell 1} - \delta_{\ell 2}$ and $V = e[v(0) - v(d)] = e\mathcal{E}d$ is the total electric potential energy difference between the graphene layers. Following the convention of Ref. (NETO *et al.*, 2009), we will denominate V as electric bias, for short, in subsequent discussions.

2.5 Hamiltonian diagonalization and band structure calculations

Gathering Eqs. (2.13,2.21), we obtain the total Hamiltonian of the non-interacting p_z electrons of TBG under a vertical electric field

$$\mathcal{H}_0 = \mathcal{H}_{\mathrm{TB}} + \mathcal{H}_V = \sum_{\mathbf{k}}^{\mathrm{BZ}}\sum_{\ell\ell'}\sum_{\boldsymbol{\delta}_\ell\boldsymbol{\delta}_{\ell'}} h_{\boldsymbol{\delta}_\ell\boldsymbol{\delta}_{\ell'}}(\mathbf{k}) b^\dagger_{\mathbf{k}\boldsymbol{\delta}_\ell} b_{\mathbf{k}\boldsymbol{\delta}_{\ell'}}, \tag{2.22}$$

where we defined the matrix element

$$h_{\boldsymbol{\delta}_\ell\boldsymbol{\delta}_{\ell'}}(\mathbf{k}) = \frac{V}{2} s_\ell \delta_{\ell\ell'}\delta_{\boldsymbol{\delta}_\ell\boldsymbol{\delta}_{\ell'}} + \sum_{\mathbf{R}} e^{\mathrm{i}\mathbf{k}\cdot(\mathbf{R}+\boldsymbol{\delta}_\ell-\boldsymbol{\delta}_{\ell'})} t(\mathbf{R}+\boldsymbol{\delta}_\ell-\boldsymbol{\delta}_{\ell'}). \tag{2.23}$$

To diagonalize the Hamiltonian (2.22), we introduce the Bloch operator

$$a^\dagger_{n\mathbf{k}} = \sum_{\boldsymbol{\delta}_\ell} u_{n\boldsymbol{\delta}_\ell}(\mathbf{k}) b^\dagger_{\mathbf{k}\boldsymbol{\delta}_\ell}, \tag{2.24}$$

where n is the band label and the Bloch functions $u_{n\boldsymbol{\delta}_\ell}(\mathbf{k})$ form a orthonormal basis. The inverse relation

$$b^\dagger_{\mathbf{k}\boldsymbol{\delta}_\ell} = \sum_{n} u^*_{n\boldsymbol{\delta}_\ell}(\mathbf{k}) a^\dagger_{n\mathbf{k}} \tag{2.25}$$

is guaranteed by the orthonormality of the basis of functions $u_{n\boldsymbol{\delta}_\ell}(\mathbf{k})$ in both the indices n and $\boldsymbol{\delta}_\ell$:

$$\sum_{n} u^*_{n\boldsymbol{\delta}_\ell}(\mathbf{k}) u_{n\boldsymbol{\delta}_{\ell'}}(\mathbf{k}) = \delta_{\boldsymbol{\delta}_\ell\boldsymbol{\delta}_{\ell'}}, \tag{2.26}$$

$$\sum_{\boldsymbol{\delta}_\ell} u^*_{n\boldsymbol{\delta}_\ell}(\mathbf{k}) u_{n'\boldsymbol{\delta}_\ell}(\mathbf{k}) = \delta_{nn'}. \tag{2.27}$$

Substituting (2.25) in (2.22) gives

$$\mathcal{H}_0 = \sum_{\mathbf{k}}^{\mathrm{BZ}} \sum_{\ell\ell'} \sum_{\boldsymbol{\delta}_\ell \boldsymbol{\delta}_{\ell'}} \sum_{nn'} h_{\boldsymbol{\delta}_\ell \boldsymbol{\delta}_{\ell'}}(\mathbf{k}) u^*_{n\boldsymbol{\delta}_\ell}(\mathbf{k}) u_{n'\boldsymbol{\delta}_{\ell'}}(\mathbf{k}) a^\dagger_{n\mathbf{k}} a_{n'\mathbf{k}}. \tag{2.28}$$

The procedure of substituting $c^\dagger_{\mathbf{R}+\boldsymbol{\delta}_\ell}$ operators by $a^\dagger_{n\mathbf{k}}$ operators through Eqs. (2.10,2.25) and simplifying $\sum_{\mathbf{R}}$ sums through Eq. (2.12) will be implicitly performed several times throughout this work, every time we need to carry out Hamiltonian terms.

Since $\mathcal{H}_0$ must be diagonal in the basis $a^\dagger_{n\mathbf{k}}$, Eq. (2.28) can be splitted into the pair of equations

$$\sum_{\ell\ell'} \sum_{\boldsymbol{\delta}_\ell \boldsymbol{\delta}_{\ell'}} h_{\boldsymbol{\delta}_\ell \boldsymbol{\delta}_{\ell'}}(\mathbf{k}) u^*_{n\boldsymbol{\delta}_\ell}(\mathbf{k}) u_{n'\boldsymbol{\delta}_{\ell'}}(\mathbf{k}) = E_{n\mathbf{k}} \delta_{nn'}, \tag{2.29a}$$

$$\mathcal{H}_0 = \sum_{\mathbf{k}}^{\mathrm{BZ}} \sum_{n} E_{n\mathbf{k}} a^\dagger_{n\mathbf{k}} a_{n\mathbf{k}}. \tag{2.29b}$$

The Hamiltonian in diagonal form (2.29b) will be important for further derivations in this work. The eigenvalues $E_{n\mathbf{k}}$ describe the energy bands of the system. On the other hand, we need to solve the eigenvalue problem (2.29a) in order to calculate the energy bands and Bloch functions. Using Eq. (2.27), we can rewrite Eq. (2.29a) in the standard form

$$\sum_{\ell' \boldsymbol{\delta}_{\ell'}} h_{\boldsymbol{\delta}_\ell \boldsymbol{\delta}_{\ell'}}(\mathbf{k}) u_{n\boldsymbol{\delta}_{\ell'}}(\mathbf{k}) = E_{n\mathbf{k}} u_{n\boldsymbol{\delta}_\ell}(\mathbf{k}), \tag{2.30}$$

for matrix elements indexed by $\boldsymbol{\delta}_\ell$ and $\boldsymbol{\delta}_{\ell'}$.

To actually solve the eigenvalue problem (2.30) numerically, explicit values for $\mathbf{k}$ must be sampled. Given the reciprocal lattice $\mathbf{G} = m\mathbf{G}_1 + n\mathbf{G}_2$ $(m, n \in \mathbb{Z})$ and the primitive vectors

$$\mathbf{G}_1 = 2\pi \frac{\mathbf{L}_2 \times \mathbf{e}_z}{|\mathbf{L}_1 \times \mathbf{L}_2|}, \tag{2.31a}$$

$$\mathbf{G}_2 = 2\pi \frac{\mathbf{e}_z \times \mathbf{L}_1}{|\mathbf{L}_1 \times \mathbf{L}_2|}. \tag{2.31b}$$

The resulting BZ of TBG is shown in Fig. 2.3, with high symmetry points located at the hexagon center $\boldsymbol{\Gamma} = \mathbf{0}$, the vertices $\mathbf{K}$ and the edge midpoints $\mathbf{M}$. We emphasize that all BZ vertices and midpoints are equivalent. For subsequent calculations in momentum space, we sampled $\mathbf{k}$-points in the sampling region highlighted in Fig. 2.3, unless stated otherwise. This region is another valid reciprocal unit cell for the material. For simplicity, we used rectangular grids with N_i sampling points in the $i = x', y'$ directions. The

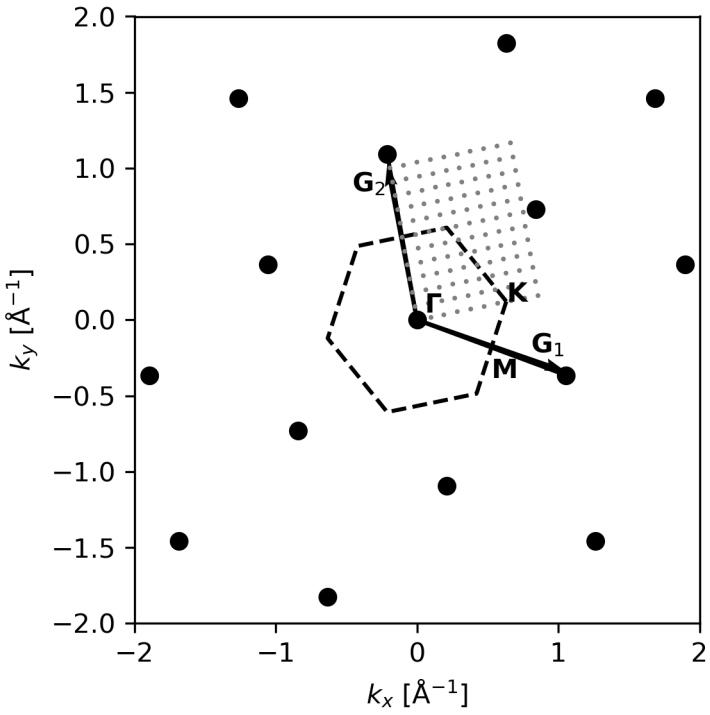

FIGURE 2.3 – (Color online) Reciprocal lattice associated with TBG. In order to explicitly draw the lattice, we arbitrated a twist angle of $\theta(1,1) \approx 21.8°$. The big dots are the lattice points $\mathbf{G} = m\mathbf{G}_1 + n\mathbf{G}_2$ ($m, n \in \mathbb{Z}$), the vectors $\mathbf{G}_{1,2}$ are the primitive vectors of the lattice, and the small dots are the sampled points (2.32). For illustrative purposes, unrealistically small values of $N_{x',y'}$ were used. Some high-symmetry points are indicated ($\mathbf{\Gamma}$, $\mathbf{K}$, $\mathbf{M}$).

sampling points are written explicitly as

$$\mathbf{k}_{n_{x'}n_{y'}} = \left(\frac{n_{x'}}{N_{x'}}\frac{\sqrt{3}}{2}\mathbf{G}_2 \cdot \mathbf{e}_y + \frac{n_{y'}}{N_{y'}}\mathbf{G}_2 \cdot \mathbf{e}_x\right)\mathbf{e}_x + \left(\frac{n_{y'}}{N_{y'}}\mathbf{G}_2 \cdot \mathbf{e}_y - \frac{n_{x'}}{N_{x'}}\frac{\sqrt{3}}{2}\mathbf{G}_2 \cdot \mathbf{e}_x\right)\mathbf{e}_y, \quad (2.32)$$

where $n_i = 0, 1, 2, \ldots, N_i - 1$. The total number of sampling points $N_{\mathbf{k}} = N_{x'}N_{y'}$ will also act as the number of unit cells that constitute our material. Moreover, it will be treated as a convergence parameter. As $N_{\mathbf{k}}$ increases, we expect that our calculations converge.

2.6 Results

Using the tight-binding model derivated in this chapter, we investigated the interplay of twist angle, electric bias, and vertical pressure in TBG. The later is mimicked by varying the interlayer distance d away from the equilibrium position $d_0 = 3.35$ Å. For sufficiently small unit cells, the eigenvalue problem (2.30) can be solved completely using a numerical algorithm, for each sampled $\mathbf{k}$-point in agreement with (2.32). This allows us to calculate all the energy bands $E_{n\mathbf{k}}$ and, therefore, we say that the Hamiltonian (2.22) can be fully diagonalized numerically in momentum space, in agreement with (2.29b).

In Fig. 2.4 we show the band gap of TBG for all the twist angles [Eq. (2.4)] that generate unit cells of less than 500 atoms as a function of electric bias and interlayer distance. The combined effect of twist, electric bias, and pressure can open band gaps of up to 200 meV, which turns TBG into a narrow gap semiconductor. Twist angles of the form $\theta(1, 3k)$ ($k \in \mathbb{Z}$) show a particularly convenient gap profile. In general, the gap of these structures increases as a function of decreasing d until some optimal value where the gap is maximum. This optimal point is brought closer to the equilibrium level $d = d_0$ as V increases. This property is useful since it shows that applying an electric bias is an easy way of decreasing the necessary pressure to maximize the band gap, which is important for experimental purposes. In Fig. 2.4 we also show, however, that the gap opening is highly sensible on the twist angle, which by itself can be tough to accurately control in an experimental setting and might make the reproduction of this result a bit challenging. On the other hand, since experiments with TBG lattices for twist angles as low as 1.1° were already reported in the literature (CAO *et al.*, 2018), we are confident that the lattices being mentioned in Fig. 2.4 can be feasibly achieved experimentally.

The next step was to fix a set of θ, V, d parameters, in order to study exciton formation. In Fig. 2.5 we present the band structure of TBG for $\theta(1, 6) \approx 46.8°$, $V = 3$ eV and $d = 2.8$ Å, through the path $\mathbf{\Gamma} - \mathbf{M} - \mathbf{K} - \mathbf{\Gamma}$ (see Fig. 2.3). For this choice of parameters, TBG becomes a semiconductor with an estimated gap of around 90 meV. The bands are highly hybridized between different layers near the Fermi level, which suggests that the formation of excitons might not be clearly intralayer nor interlayer. This is further investigated on Section 4.3 of this work.

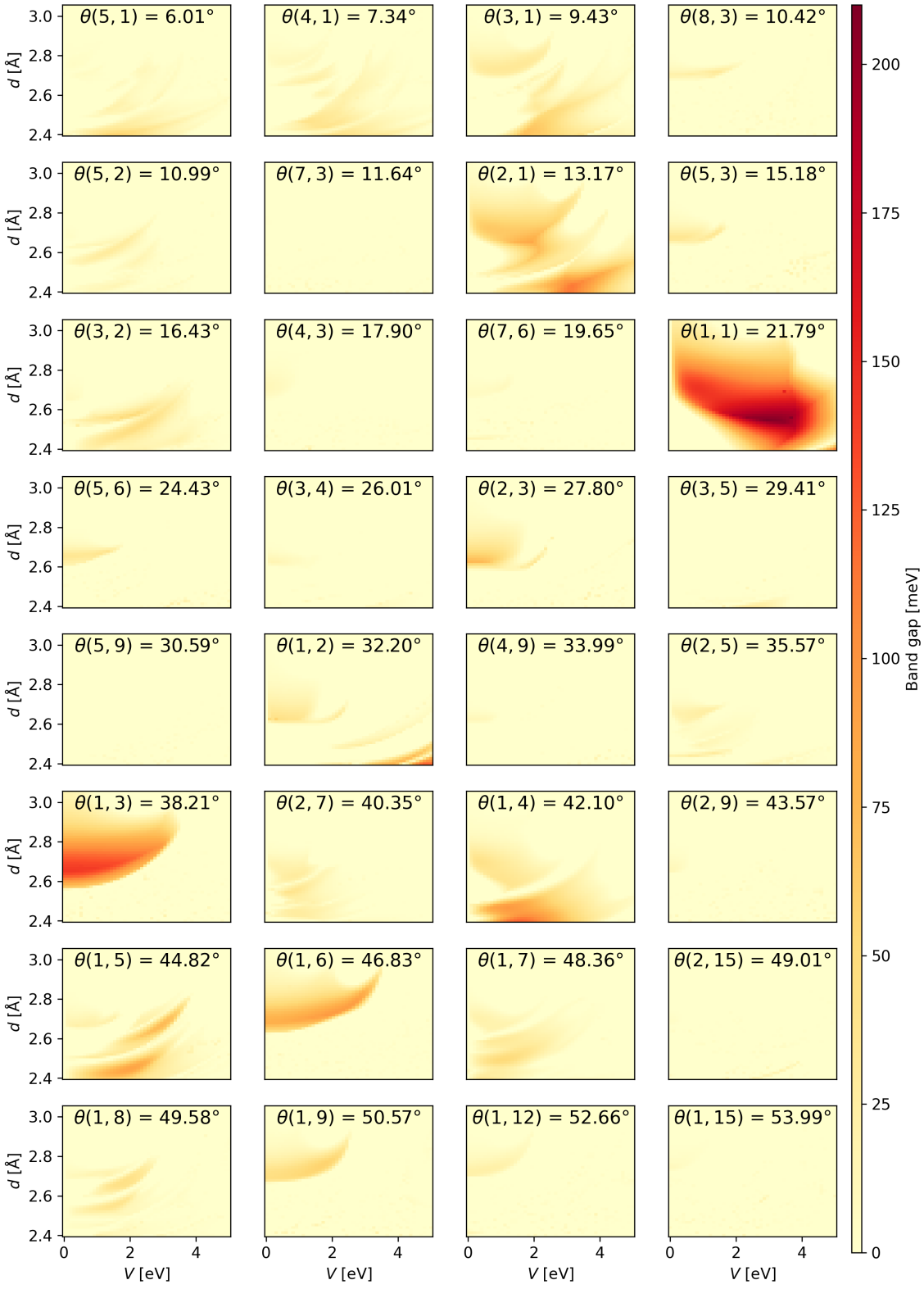

FIGURE 2.4 – (Color online) Band gap of TBG for twist angles that generate commensurate unit cells with less than 500 atoms. The band gap is evaluated as a function of electric bias V and interlayer distance d. The decreasing of the later mimicks the application of vertical pressure.

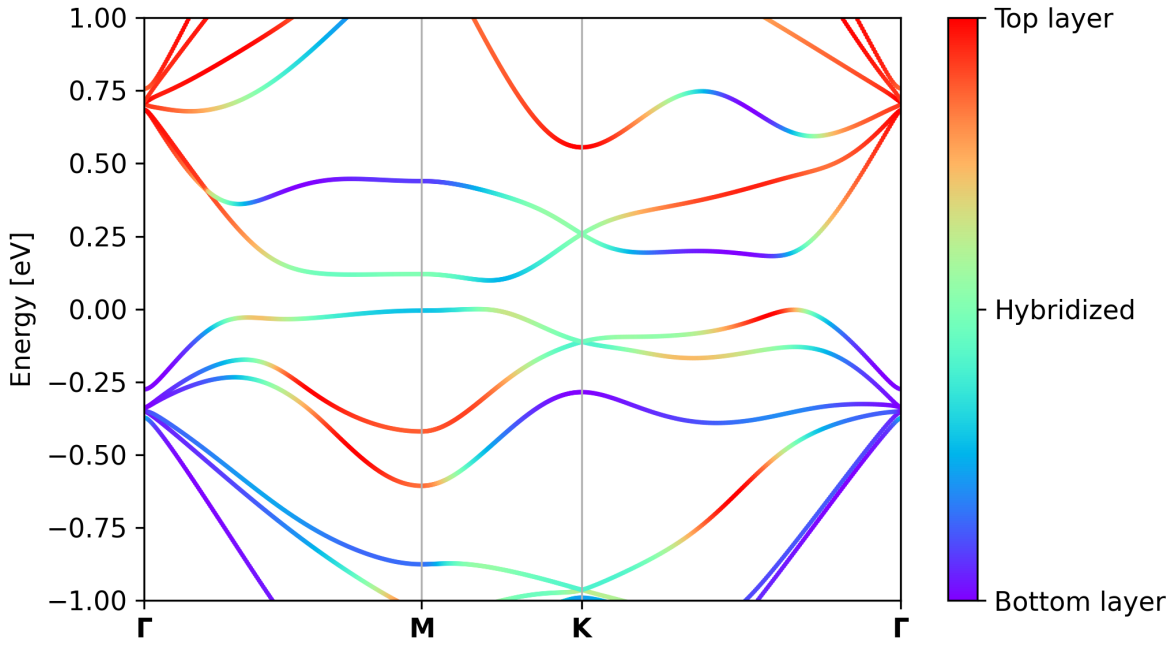

FIGURE 2.5 – (Color online) Electronic band structure of TBG for $\theta(1,6) \approx 46.8°$, $V = 3$ eV and $d = 2.8$ Å. The energy reference is the Fermi level, set to $E_F = 0$ eV in the vertical axis. The color map indicates layer composition of either the bottom ($\ell = 1$) or top ($\ell = 2$) layers. We focus our attention on the band gap opening and, moreover, on the layer composition and dispersion profile of the highest valence and lowest conduction bands, where the interband transitions associated with the formation of excitons are more likely to occur.

3 Dielectric screening

In Chapter 2, the electronic structure of single-particle excitations, considering non-interacting electrons, was described through the tight-binding formalism. To describe exciton formation, we must add many-body interactions to this model, *i.e.*, electron-electron and electron-hole interactions. Before discussing how we approach this problem, in this chapter, we define the static dielectric function of TBG, denoted by the letter ϵ, which will describe how the system is polarized due to the application of an external electric field and how this polarization screens the electrostatic response of the system itself. In this work, the dielectric function is calculated in the context of the Random Phase Approximation (RPA) (BOHM; PINES, 1951; PINES; BOHM, 1952; BOHM; PINES, 1953) for a periodic system (ADLER, 1962; WISER, 1963).

3.1 Fourier transforms

For a system of electrons perturbed by a dynamic external potential ϕ_{ext}, the RPA states that the electrons will respond to ϕ_{ext} and a screening potential ϕ_{scr} induced by electrons themselves. Like any well-behaved 1D function, the time dependence of ϕ_{ext} and other relevant physical quantities can be Fourier transformed to frequency domain through the convention

$$\phi_{\text{ext}}(\mathbf{r}_{\parallel}, z, t) = \int \frac{\mathrm{d}\omega}{2\pi}\, e^{-\mathrm{i}\omega t}\phi_{\text{ext}}(\mathbf{r}_{\parallel}, z, \omega), \tag{3.1}$$

with the inverse relation

$$\phi_{\text{ext}}(\mathbf{r}_{\parallel}, z, \omega) = \int \mathrm{d}t\, e^{\mathrm{i}\omega t}\phi_{\text{ext}}(\mathbf{r}_{\parallel}, z, t), \tag{3.2}$$

where $\mathbf{r}_{\parallel}$ is an in-plane real space vector, z is the out-of-plane coordinate, t is time and ω is frequency. This gives the spectral composition of ϕ_{ext} in terms of pure harmonic components as a function of the oscillation frequency ω. As will become evident in subsequent discussions, we will be solely concerned with the electronic response in the static regime, where ω goes to zero. Physically, this means the external potential must be constant in

time.

Similarly, the in-plane real space dependence of ϕ_{ext} and any other relevant one-body quantities are Fourier transformed to momentum domain through the convention

$$\phi_{\text{ext}}(\mathbf{r}_\parallel, z) = \frac{1}{\mathcal{S}} \sum_{\mathbf{k}} e^{\mathrm{i}\mathbf{k}\cdot\mathbf{r}_\parallel} \phi_{\text{ext}}(\mathbf{k}, z), \tag{3.3}$$

where $\mathcal{S}$ is the total surface area of the 2D material. In the case of TBG, we have $\mathcal{S} = N_{\mathbf{k}} \|\mathbf{L}_1 \times \mathbf{L}_2\|$. The inverse relation is

$$\phi_{\text{ext}}(\mathbf{k}, z) = \int \mathrm{d}\mathbf{r}_\parallel \, e^{-\mathrm{i}\mathbf{k}\cdot\mathbf{r}_\parallel} \phi_{\text{ext}}(\mathbf{r}_\parallel, z). \tag{3.4}$$

For ease of notation, we will use $\mathbf{r} = \mathbf{r}_\parallel$ and a superindex ℓ to indicate the z-dependence restricted to $z = 0$ ($\ell = 1$) and $z = d$ ($\ell = 2$) from now on. The dielectric function is defined as the function that satisfies

$$\phi^\ell_{\text{ext}}(\mathbf{r}) = \int \mathrm{d}\mathbf{r}' \epsilon^{\ell\ell'}(\mathbf{r}, \mathbf{r}') \phi^{\ell'}(\mathbf{r}'), \tag{3.5}$$

where $\phi = \phi_{\text{ext}} + \phi_{\text{scr}}$. The inverse dielectric function is defined through the orthogonality relation

$$\int \mathrm{d}\mathbf{r} \, \epsilon^{\ell\ell'}(\mathbf{r}_1, \mathbf{r}) \epsilon^{-1\,\ell\ell'}(\mathbf{r}, \mathbf{r}_2) = \delta_{\ell\ell'} \delta(\mathbf{r}_1 - \mathbf{r}_2), \tag{3.6}$$

which allows us to rewrite (3.5) as

$$\phi^\ell(\mathbf{r}) = \int \mathrm{d}\mathbf{r}' \epsilon^{-1\,\ell\ell'}(\mathbf{r}, \mathbf{r}') \phi^\ell_{\text{ext}}(\mathbf{r}'). \tag{3.7}$$

The dielectric function (and analogously, its inverse) is Fourier transformed through the convention

$$\epsilon^{\ell\ell'}(\mathbf{r}, \mathbf{r}') = \frac{1}{\mathcal{S}^2} \sum_{\mathbf{k}\mathbf{k}'} e^{\mathrm{i}\mathbf{k}\cdot\mathbf{r}} \epsilon^{\ell\ell'}(\mathbf{k}, \mathbf{k}') e^{-\mathrm{i}\mathbf{k}'\cdot\mathbf{r}'}, \tag{3.8}$$

whose inverse is

$$\epsilon^{\ell\ell'}(\mathbf{k}, \mathbf{k}') = \int \mathrm{d}\mathbf{r} \int \mathrm{d}\mathbf{r}' e^{-\mathrm{i}\mathbf{k}\cdot\mathbf{r}} \epsilon^{\ell\ell'}(\mathbf{r}, \mathbf{r}') e^{\mathrm{i}\mathbf{k}'\cdot\mathbf{r}'}. \tag{3.9}$$

The orthogonality relation becomes

$$\sum_{\mathbf{k}} \epsilon^{\ell\ell'}(\mathbf{k}_1, \mathbf{k}) \epsilon^{-1\,\ell\ell'}(\mathbf{k}, \mathbf{k}_2) = \delta_{\ell\ell'} \delta_{\mathbf{k}_1\mathbf{k}_2}. \tag{3.10}$$

Using the Fourier transform conventions (3.3,3.8), we can take (3.5,3.7) to momentum space:

$$\phi^\ell_{\text{ext}}(\mathbf{k}) = \sum_{\mathbf{k}'} \epsilon(\mathbf{k}, \mathbf{k}') \phi^\ell(\mathbf{k}'), \tag{3.11a}$$

$$\phi^{\ell}(\mathbf{k}) = \sum_{\mathbf{k}'} \epsilon^{-1}(\mathbf{k}, \mathbf{k}')\phi^{\ell}_{\text{ext}}(\mathbf{k}'). \tag{3.11b}$$

Equations (3.11a, 3.11b) relate the external and total potentials in momentum space through the direct and inverse dielectric functions. They will be the starting point for the discussions of the next Section, where we will establish the formalism necessary to perform dielectric function calculations in momentum space.

3.2 Formalism

In this section, we present a procedure derived to express the dielectric function solely in terms of eigenenergies $E_{n\mathbf{k}}$ and overlap of wavefunctions $u_{n\boldsymbol{\delta}}(\mathbf{k})$ of the unperturbed system, described by the Hamiltonian $\mathcal{H}_0$ as discussed in Chapter 2. This is an adaptation of the works of Refs. (ADLER, 1962; WISER, 1963) for layered 2D materials. We will consider that the potential at $\mathbf{k}$ is only affected by $\mathbf{k}' = \mathbf{k}$ and its periodical repetitions, which can be included in our model by restricting the dielectric function to

$$\epsilon^{\ell\ell'}(\mathbf{k}, \mathbf{k}') = \sum_{\mathbf{G}_1} \epsilon^{\ell\ell'}(\mathbf{k}, \mathbf{k}')\delta_{\mathbf{k}+\mathbf{G}_1,\mathbf{k}'}. \tag{3.12}$$

The remaining contributions are assumed to average out to zero, which is well justified in the context of the RPA. In fact, we could go a step further and restrict the screening contributions to the dominant term $\mathbf{G}_1 = 0$ ($\mathbf{k}' = \mathbf{k}$) only, meaning that the dielectric function would be approximated to a local function in momentum space. However, the formulation (3.12) allows us to be a bit more broad, and inspect how the terms $\mathbf{G}_1 \neq 0$ affect the screening if necessary. Expanding $\mathbf{k}, \mathbf{k}'$ as $\mathbf{k} = \mathbf{q} + \mathbf{G}, \mathbf{k}' = \mathbf{q}' + \mathbf{G}'$, with $\mathbf{q}, \mathbf{q}'$ wavevectors restricted to the BZ and $\mathbf{G}, \mathbf{G}'$ reciprocal lattice vectors, (3.12) can be rewritten as

$$\epsilon^{\ell\ell'}(\mathbf{q}+\mathbf{G}, \mathbf{q}'+\mathbf{G}') = \sum_{\mathbf{G}_1} \epsilon^{\ell\ell'}(\mathbf{q}+\mathbf{G}, \mathbf{q}'+\mathbf{G}')\delta_{\mathbf{q}+\mathbf{G}+\mathbf{G}_1,\mathbf{q}'+\mathbf{G}'} \tag{3.13}$$

$$= \sum_{\mathbf{G}'_1} \epsilon^{\ell\ell'}(\mathbf{q}+\mathbf{G}, \mathbf{q}'+\mathbf{G}')\delta_{\mathbf{q}+\mathbf{G}'_1,\mathbf{q}'} \tag{3.14}$$

$$= \epsilon^{\ell\ell'}_{\mathbf{G}\mathbf{G}'}(\mathbf{q})\delta_{\mathbf{q},\mathbf{q}'}, \tag{3.15}$$

where we defined $\epsilon^{\ell\ell'}_{\mathbf{G}\mathbf{G}'}(\mathbf{q}) = \epsilon^{\ell\ell'}(\mathbf{q}+\mathbf{G}, \mathbf{q}+\mathbf{G}')$. Using this result, we rewrite (3.10) as

$$\sum_{\ell\mathbf{G}} \epsilon^{\ell_1\ell}_{\mathbf{G}_1\mathbf{G}}(\mathbf{q})\epsilon^{-1}{}^{\ell\ell_2}_{\mathbf{G}\mathbf{G}_2}(\mathbf{q}) = \delta_{\ell_1\ell_2}\delta_{\mathbf{G}_1\mathbf{G}_2}, \tag{3.16}$$

and, subsequently, (3.11a, 3.11b) become

$$\phi^{\ell}_{\text{ext}}(\mathbf{q}+\mathbf{G}) = \sum_{\ell'\mathbf{G}'} \epsilon^{\ell\ell'}_{\mathbf{G}\mathbf{G}'}(\mathbf{q})\phi^{\ell'}(\mathbf{q}+\mathbf{G}'), \tag{3.17a}$$

$$\phi^{\ell}(\mathbf{q}+\mathbf{G}) = \sum_{\ell'\mathbf{G}'} {\epsilon^{-1}}^{\ell\ell'}_{\mathbf{G}\mathbf{G}'}(\mathbf{q})\phi^{\ell'}_{\text{ext}}(\mathbf{q}+\mathbf{G}'). \tag{3.17b}$$

When excitons are formed in TBG, the electron-hole interaction is screened by its surroundings. This effect must be taken into account in order to describe the excitonic spectrum accurately. As mentioned previously, in this section we present a formalism adapted from Refs. (ADLER, 1962; WISER, 1963) to take the screening effect into account through a description of the linear electronic response of the p_z electrons of TBG in light of the RPA. The electronic distribution fluctuations around the ground state are associated to a certain induced potential ϕ_{ind}. To study how excitons are formed in this system, one might think they would need to know the exact form of ϕ_{ext}. We will, however, approach this problem in another way, by associating a dielectric function that will establish a direct relation between ϕ_{ext} and the total potential $\phi = \phi_{\text{ext}} + \phi_{\text{ind}}$.

We treat each carbon site of TBG as a point charge, such that variations in charge density due to fluctuations near the Fermi level can be written as

$$\sigma_1(\mathbf{r})\delta(z) + \sigma_2(\mathbf{r})\delta(z-d), \tag{3.18}$$

where $\sigma_\ell(\mathbf{r})$ is the surface charge density fluctuation of layer ℓ. The induced potential is obtained through the solution of the Poisson equation for the charge density given by (3.18):

$$\nabla^2\phi_{\text{ind}}(\mathbf{r},z) = -\frac{1}{\epsilon_0}\left[\sigma_1(\mathbf{r})\delta(z) + \sigma_2(\mathbf{r})\delta(z-d)\right]. \tag{3.19}$$

We Fourier transform this equation and obtain the solution in momentum space

$$\phi^{\ell}_{\text{ind}}(\mathbf{k}) = \sum_{\ell'} \phi_0^{\ell\ell'}(k)\sigma_{\ell'}(\mathbf{k}), \tag{3.20}$$

where ϕ_0 is the Coulomb potential without screening

$$\phi_0^{\ell\ell'}(k) = \frac{\delta_{\ell\ell'} + (1-\delta_{\ell\ell'})e^{-kd}}{2\epsilon_0 k}, \tag{3.21}$$

denominated bare Coulomb potential. This potential acts on the system through the

one-body Hamiltonian

$$\mathcal{H}_{\text{ind}} = -e \sum_{\ell \boldsymbol{\delta}_\ell} \sum_{\mathbf{R}} \phi^\ell(\mathbf{R} + \boldsymbol{\delta}_\ell) c^\dagger_{\mathbf{R}+\boldsymbol{\delta}_\ell} c_{\mathbf{R}+\boldsymbol{\delta}_\ell} \tag{3.22}$$

$$= -\frac{e}{\mathcal{S}} \sum_{\mathbf{q}}^{\text{BZ}} \sum_{\ell} \sum_{\mathbf{G}} \phi^\ell(\mathbf{q} + \mathbf{G}) \sum_{\mathbf{k}}^{\text{BZ}} \sum_{nn'} M_\ell^{nn'}(\mathbf{k}, \mathbf{q}, \mathbf{G}) a^\dagger_{n\mathbf{k}} a_{n'\mathbf{k}+\mathbf{q}}, \tag{3.23}$$

where we defined the overlap term

$$M_\ell^{nn'}(\mathbf{k}, \mathbf{q}, \mathbf{G}) = \sum_{\boldsymbol{\delta}_\ell} u^*_{n\boldsymbol{\delta}_\ell}(\mathbf{k}) e^{\mathrm{i}\mathbf{G}\boldsymbol{\delta}_\ell} u_{n'\boldsymbol{\delta}_\ell}(\mathbf{k} + \mathbf{q}). \tag{3.24}$$

Now we consider the Liouville equation

$$-\mathrm{i}\hbar \partial_t \rho = [\mathcal{H}, \rho], \tag{3.25}$$

one of the fundamental equations of statistical mechanics (HUANG, 1987). This equation describes the evolution of a quantum system of particles in terms of the distribution function ρ in phase space associated to a Hamiltonian $\mathcal{H}$. For the unperturbed system, we have $\mathcal{H} = \mathcal{H}_0$ and $\rho = \rho_0$, where ρ_0 is the well known distribution of the system of independent electrons following the Pauli exclusion principle. Thus, we can write

$$\rho_0 |n\mathbf{k}\rangle = f(E_{n\mathbf{k}}) |n\mathbf{k}\rangle, \tag{3.26}$$

where $f(E)$ is the Fermi-Dirac distribution

$$f(E) = \frac{1}{\exp\{(E - E_F)/k_B T\} + 1}, \tag{3.27}$$

where k_B is the Boltzmann constant and T is temperature. Notice that, as T approaches zero, Eq. (3.27) simplifies to

$$f(E) = \begin{cases} 1, \text{ if } E < E_F, \\ 1/2, \text{ if } E = E_F, \\ 0, \text{ if } E > E_F. \end{cases} \tag{3.28}$$

This equation shows that, in the ground state ($T = 0$), only the states below the Fermi level (namely the valence states) are occupied. The states above the Fermi level (namely the conduction states) are all unoccupied.

The unperturbed distribution ρ_0 commutes with $\mathcal{H}_0$ since (2.29b,3.26) show they are simultaneously diagonalized by the basis of Bloch states $|n\mathbf{k}\rangle$. For this reason, the unper-

turbed distribution remains static in time since the Liouville equation (3.25) in this case can be simplified to

$$-\mathrm{i}\hbar\partial_t\rho_0 = [\mathcal{H}_0, \rho_0] = 0. \tag{3.29}$$

Now we set $\mathcal{H} = \mathcal{H}_0 + \mathcal{H}_{\text{ind}}$ and consider fluctuations ρ_{ind} around the distribution ρ_0 of the unperturbed system $\mathcal{H}_0$, whose eigenstates are $|n\mathbf{k}\rangle = a^\dagger_{n\mathbf{k}}|0\rangle$. Thus, $\rho = \rho_0 + \rho_{\text{ind}}$. On the other hand, ρ_{ind} is closely related with fluctuations in the charge density through

$$\sigma_\ell(\mathbf{r}) = -e\sum_{\boldsymbol{\delta}_\ell\mathbf{R}} \delta(\mathbf{r}-\mathbf{R}-\boldsymbol{\delta}_\ell)\langle\mathbf{R}+\boldsymbol{\delta}_\ell|\rho_{\text{ind}}|\mathbf{R}+\boldsymbol{\delta}_\ell\rangle, \tag{3.30}$$

which is Fourier transformed to

$$\sigma_\ell(\mathbf{q}+\mathbf{G}) = -e\sum_{\mathbf{k}}^{\text{BZ}}\sum_{nn'}\left(M_\ell^{nn'}(\mathbf{k},\mathbf{q},\mathbf{G})\right)^*\langle n\mathbf{k}|\rho_{\text{ind}}|n'\mathbf{k}+\mathbf{q}\rangle. \tag{3.31}$$

To explicit the matrix elements of ρ_{ind} in the basis $|n\mathbf{k}\rangle$, we recognize that, as a first order approximation, the differential equation (3.25) can be linearized by setting ρ_{ind} proportional to the perturbation $\mathcal{H}_{\text{ind}}$. Under this consideration, the commutator $[\mathcal{H}_{\text{ind}}, \rho_{\text{ind}}]$ will vanish, and so will $[\mathcal{H}_0, \rho_0]$ and $\partial_t\rho_0$ as we recall from (3.29). Thus,

$$-\mathrm{i}\hbar\partial_t\rho_{\text{ind}} = [\mathcal{H}_0, \rho_{\text{ind}}] + [\mathcal{H}_{\text{ind}}, \rho_0]. \tag{3.32}$$

The final step is to recognize that, in the static approximation, ρ_{ind} will vary slowly. Therefore, setting $\partial_t\rho_{\text{ind}} \approx 0$ gives

$$\langle n\mathbf{k}|\rho_{\text{ind}}|n'\mathbf{k}+\mathbf{q}\rangle = \frac{f(E_{n\mathbf{k}}) - f(E_{n'\mathbf{k}+\mathbf{q}})}{E_{n\mathbf{k}} - E_{n'\mathbf{k}+\mathbf{q}}}\langle n\mathbf{k}|\mathcal{H}_{\text{ind}}|n'\mathbf{k}+\mathbf{q}\rangle, \tag{3.33}$$

which we apply in (3.31) and explicit the matrix elements $\langle n\mathbf{k}|\,\mathcal{H}_{\text{ind}}\,|n'\mathbf{k}+\mathbf{q}\rangle$ by recalling (3.23) to obtain

$$\sigma_\ell(\mathbf{q}+\mathbf{G}) = \frac{e^2}{\mathcal{S}}\sum_{\mathbf{k}}^{\text{BZ}}\sum_{nn'}\left(M_\ell^{nn'}(\mathbf{k},\mathbf{q},\mathbf{G})\right)^*\frac{f(E_{n\mathbf{k}}) - f(E_{n'\mathbf{k}+\mathbf{q}})}{E_{n\mathbf{k}} - E_{n'\mathbf{k}+\mathbf{q}}}\times \\ \times\sum_{\ell'}\sum_{\mathbf{G}'}\phi^{\ell'}(\mathbf{q}+\mathbf{G}')M_{\ell'}^{nn'}(\mathbf{k},\mathbf{q},\mathbf{G}'). \tag{3.34}$$

Merging (3.20) with (3.34) and rearranging some terms results in

$$\phi^{\ell}_{\mathrm{ind}}(\mathbf{q}+\mathbf{G}) = \frac{e^2}{\mathcal{S}} \sum_{\ell'\mathbf{G}'} \phi^{\ell'}(\mathbf{q}+\mathbf{G}') \sum_{\ell''} \phi_0^{\ell\ell''}(|\mathbf{q}+\mathbf{G}|)\times \\ \times \sum_{nn'} \sum_{\mathbf{k}}^{\mathrm{BZ}} \Big(M^{nn'}_{\ell''}(\mathbf{k},\mathbf{q},\mathbf{G})\Big)^* \frac{f(E_{n\mathbf{k}}) - f(E_{n'\mathbf{k}+\mathbf{q}})}{E_{n\mathbf{k}} - E_{n'\mathbf{k}+\mathbf{q}}} M^{nn'}_{\ell'}(\mathbf{k},\mathbf{q},\mathbf{G}'), \quad (3.35)$$

which establishes a relation between ϕ_{ind} and ϕ solely in terms of energies and overlap of wavefunctions both associated to the unperturbed system alone. Putting this aside for a moment, we recall that $\phi = \phi_{\mathrm{ext}} + \phi_{\mathrm{ind}}$ and use the dielectric function definition (3.17a) to derive another relation between ϕ_{ind} and ϕ:

$$\phi^{\ell}_{\mathrm{ind}}(\mathbf{q}+\mathbf{G}) = \sum_{\ell'\mathbf{G}'} \phi^{\ell'}(\mathbf{q}+\mathbf{G}') \left[\delta_{\ell\ell'}\delta_{\mathbf{G}\mathbf{G}'} - \epsilon^{\ell\ell'}_{\mathbf{G}\mathbf{G}'}(\mathbf{q})\right]. \quad (3.36)$$

Now we compare Eqs. (3.35, 3.36) to arrive at the final expression for the dielectric function

$$\epsilon^{\ell\ell'}_{\mathbf{G}\mathbf{G}'}(\mathbf{q}) = \delta_{\ell\ell'}\delta_{\mathbf{G}\mathbf{G}'} - \frac{e^2}{\mathcal{S}} \sum_{\ell''} \phi_0^{\ell\ell''}(|\mathbf{q}+\mathbf{G}|)\times \\ \times \sum_{nn'} \sum_{\mathbf{k}}^{\mathrm{BZ}} \Big(M^{nn'}_{\ell''}(\mathbf{k},\mathbf{q},\mathbf{G})\Big)^* \frac{f(E_{n\mathbf{k}}) - f(E_{n'\mathbf{k}+\mathbf{q}})}{E_{n\mathbf{k}} - E_{n'\mathbf{k}+\mathbf{q}}} M^{nn'}_{\ell'}(\mathbf{k},\mathbf{q},\mathbf{G}'), \quad (3.37)$$

which can be seen as a set of matrix elements indexed by $\{\ell, \mathbf{G}\}$ and $\{\ell', \mathbf{G}'\}$. In the limit of zero temperature, we can explicit values for $f(E_{\mathbf{k}})$ using (3.28) to rewrite (3.37) as

$$\epsilon^{\ell\ell'}_{\mathbf{G}\mathbf{G}'}(\mathbf{q}) = \delta_{\ell\ell'}\delta_{\mathbf{G}\mathbf{G}'} + \frac{e^2}{\mathcal{S}} \sum_{\ell''} \phi_0^{\ell\ell''}(|\mathbf{q}+\mathbf{G}|)\times \\ \times \sum_{n_c n_v} \sum_{\mathbf{k}}^{\mathrm{BZ}} \frac{\left(M^{n_c n_v}_{\ell''}(\mathbf{k},\mathbf{q},\mathbf{G})\right)^* M^{n_c n_v}_{\ell'}(\mathbf{k},\mathbf{q},\mathbf{G}')}{E_{n_c\mathbf{k}} - E_{n_v\mathbf{k}+\mathbf{q}}} + \\ + \frac{\left(M^{n_v n_c}_{\ell''}(\mathbf{k},\mathbf{q},\mathbf{G})\right)^* M^{n_v n_c}_{\ell'}(\mathbf{k},\mathbf{q},\mathbf{G}')}{E_{n_c\mathbf{k}+\mathbf{q}} - E_{n_v\mathbf{k}}}, \quad (3.38)$$

where n_c (n_v) is a band index that sums over conduction (valence) bands only.

At last, we emphasize that, for $\mathbf{q}$ of small norm, the dominant terms $\epsilon^{\ell\ell'}_{\mathbf{0}\mathbf{0}}$ can be simplified in light of the Rytova-Keldysh potential (RYTOVA, 1967; KELDYSH, 1979) for 2D systems. In this case, it takes the form

$$\epsilon^{\ell\ell'}_{\mathbf{G}\mathbf{G}'}(\mathbf{q}) \approx (\delta_{\ell\ell'} + r_0^{\ell\ell'} q)\delta_{\mathbf{G}\mathbf{0}}\delta_{\mathbf{G}'\mathbf{0}}, \quad (3.39)$$

where $r_0^{\ell\ell'}$ are constants.

3.3 Results

The dielectric function was calculated using (3.38) restricted to the reciprocal lattice vectors $\mathbf{G} = \mathbf{G}' = \mathbf{0}$, for the TBG system defined by the parameters $\theta(1, 6) \approx 46.8°$, $V = 3$ eV and $d = 2.8$ Å. The result is presented in Fig. 3.1 for $\ell = \ell' = 0$ and $\mathbf{G} = \mathbf{G}' = \mathbf{0}$, showing a close to isotropic behavior. The remaining matrix terms manifested a very similar profile qualitatively. In Fig. 3.1, the dashed line shows the path followed by the peak of the dielectric function. We verified that the peak value strictly increases with increasing $\angle\mathbf{q}$. Given that $\mathbf{q} = (0, q_y^{\max})$, $(q_x^{\max}, 0)$ maximize the dielectric function at $q_x = 0$ and $q_y = 0$, respectively, we evaluated the ratios $\epsilon^{00}_{\mathbf{00}}(0, q_{y,max})/\epsilon^{00}_{\mathbf{00}}(q_x^{\max}, 0) \approx 1.08$ and $q_y^{\max}/q_x^{\max} \approx 1.21$. This ratios provide a rough quantitative picture for the anisotropy of the dielectric function, which forbade us to simplify the dielectric function to a $\|\mathbf{q}\|$-dependent function. Despite of that, we were able to verify that the dielectric function presents a linear dependence with respect to $\mathbf{q}$ for small $\|\mathbf{q}\|$ values and goes to 1 at $\mathbf{q} = \mathbf{0}$, in agreement with (3.39) for $r_0^{\ell\ell'} \sim 300$ Å. The exact fit value for $r_0^{\ell\ell'}$, however, is highly dependent on $\angle\mathbf{q}$, which is another indicator of anisotropy.

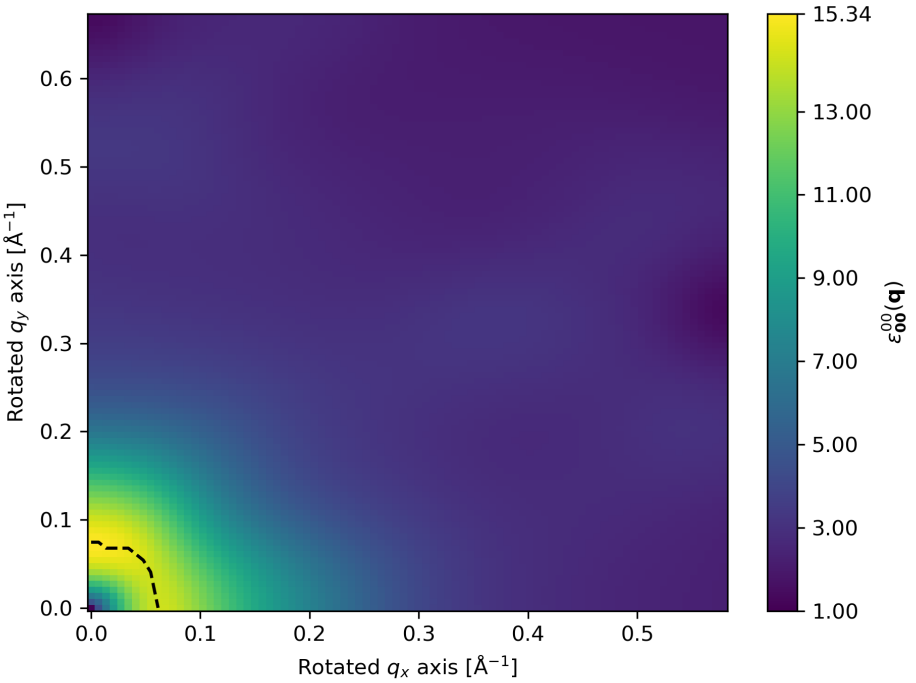

FIGURE 3.1 – (Color online) Dominant term ($\ell = \ell' = 0$, $\mathbf{G} = \mathbf{G}' = \mathbf{0}$) of the dielectric function in momentum space (3.5), as a function of the transferred momentum $\mathbf{q}$, calculated in a rectangular unit cell as shown in Fig. (2.3). The dashed line shows the path followed by the peak of the dielectric function.

4 Excitons

4.1 Dielectric screening of the electron-electron interaction

We start by following an approach very analogous to Sec. 3.2, but this time we treat the potential of any p_z electron in TBG, placed at site $\mathbf{r}_1$ and layer ℓ_1, as the "external" potential acting on another p_z electron placed at site $\mathbf{r}_2$ and layer ℓ_2. We denote this external potential by $\phi_0^{\ell_1\ell_2}(\mathbf{r}_1, \mathbf{r}_2)$ and the screened total potential by $\phi^{\ell_1\ell_2}(\mathbf{r}_1, \mathbf{r}_2)$.

The total potential can be expanded in plane waves applying the Fourier transform (3.3) with respect to the real space of $\mathbf{r}_2$ positions:

$$\phi^{\ell_1\ell_2}(\mathbf{r}_1, \mathbf{r}_2) = \frac{1}{\mathcal{S}} \sum_{\mathbf{q}}^{\mathrm{BZ}} \sum_{\mathbf{G}} \phi^{\ell_1\ell_2}(\mathbf{r}_1, \mathbf{q}+\mathbf{G}) e^{\mathrm{i}(\mathbf{q}+\mathbf{G})\cdot\mathbf{r}_2}. \tag{4.1}$$

Now we rewrite the dielectric function definition by analogy with (3.5):

$$\phi^{\ell_1\ell_2}(\mathbf{r}_1, \mathbf{q}+\mathbf{G}) = \sum_{\ell'\mathbf{G}'} {\epsilon^{-1}}_{\mathbf{G}\mathbf{G}'}^{\ell_2\ell'}(\mathbf{q}) \phi_0^{\ell_1\ell'}(\mathbf{r}_1, \mathbf{q}+\mathbf{G}'). \tag{4.2}$$

The bare Coulomb potential satisfies $\phi_0^{\ell_1\ell_2}(\mathbf{r}_1, \mathbf{r}_2) = \phi_0^{\ell_1\ell_2}(\mathbf{r}_2 - \mathbf{r}_1)$, which allow us to apply the translation property of the Fourier transform

$$\phi_0^{\ell_1\ell_2}(\mathbf{r}_1, \mathbf{q}+\mathbf{G}) = \phi_0^{\ell_1\ell_2}(|\mathbf{q}+\mathbf{G}|) e^{-\mathrm{i}|\mathbf{q}+\mathbf{G}|\cdot\mathbf{r}_1}, \tag{4.3}$$

recognizing that the Bare Coulomb potential in momentum space $\phi_0^{\ell_1\ell_2}(|\mathbf{q}+\mathbf{G}|)$ has the exact same form as (3.21). Substituting (4.2) and (4.3) on (4.1), we get

$$\phi^{\ell_1\ell_2}(\mathbf{r}_1, \mathbf{r}_2) = \frac{1}{\mathcal{S}} \sum_{\mathbf{q}}^{\mathrm{BZ}} \sum_{\mathbf{G}\mathbf{G}'} \psi_{\mathbf{G}\mathbf{G}'}^{\ell_1\ell}(\mathbf{q}) e^{\mathrm{i}(\mathbf{q}+\mathbf{G})\cdot\mathbf{r}_2} e^{-\mathrm{i}(\mathbf{q}+\mathbf{G}')\cdot\mathbf{r}_1}, \tag{4.4}$$

where we defined the screening term

$$\psi_{\mathbf{G}\mathbf{G}'}^{\ell_1\ell_2}(\mathbf{q}) = \sum_{\ell'} {\epsilon^{-1}}_{\mathbf{G}\mathbf{G}'}^{\ell_2\ell'}(\mathbf{q}) \phi_0^{\ell_1\ell'}(|\mathbf{q}+\mathbf{G}'|). \tag{4.5}$$

The interaction between p_z electrons originated from this potential is a two-body operator

$$\mathcal{H}_{\text{ee}} = -\frac{e}{2}\sum_{\ell_1\ell_2}\sum_{\boldsymbol{\delta}_{\ell_1}\boldsymbol{\delta}_{\ell_2}}\sum_{\mathbf{R}_1\mathbf{R}_2}\phi^{\ell_1\ell_2}(\mathbf{R}_1+\boldsymbol{\delta}_{\ell_1},\mathbf{R}_2+\boldsymbol{\delta}_{\ell_2})c^\dagger_{\mathbf{R}_1+\boldsymbol{\delta}_{\ell_1}}c^\dagger_{\mathbf{R}_2+\boldsymbol{\delta}_{\ell_2}}c_{\mathbf{R}_2+\boldsymbol{\delta}_{\ell_2}}c_{\mathbf{R}_1+\boldsymbol{\delta}_{\ell_1}} \tag{4.6a}$$

$$= -\frac{e}{2\mathcal{S}}\sum_{\ell_1\ell_2}\sum_{n_1n_2n_3n_4}\sum_{\mathbf{k}_1\mathbf{k}_2}\sum_{\mathbf{q}}^{\text{BZ}}\sum_{\mathbf{G}\mathbf{G}'}\psi^{\ell_1\ell_2}_{\mathbf{G}\mathbf{G}'}(\mathbf{q})(M^{n_1n_4}_{\ell_1}(\mathbf{k}_1,\mathbf{q},\mathbf{G}'))^*M^{n_2n_3}_{\ell_2}(\mathbf{k}_2,\mathbf{q},\mathbf{G})\times$$
$$\times\, a^\dagger_{n_1\mathbf{k}_1+\mathbf{q}}a^\dagger_{n_2\mathbf{k}_2}a_{n_3\mathbf{k}_2+\mathbf{q}}a_{n_4\mathbf{k}_1}, \tag{4.6b}$$

where the factor of $1/2$ is included to avoid double counting.

4.2 Semiconductor Bloch Equations

To derive the Semiconductor Bloch Equations (SBEs), we first define the full Hamiltonian

$$\mathcal{H} = \mathcal{H}_0 + \mathcal{H}_{\text{ee}} + \mathcal{H}_I, \tag{4.7}$$

where $\mathcal{H}_I$ is the dipole energy term related to the interaction of p_z electrons with the classical electric field $\boldsymbol{\mathcal{E}}$ of the incident light:

$$\mathcal{H}_I = -\sum_{\mathbf{k}}^{\text{BZ}}\boldsymbol{\mathcal{E}}\cdot\left(\mathbf{d}^*_{cv}(\mathbf{k})a^\dagger_{c,\mathbf{k}}a_{v,\mathbf{k}} + \mathbf{d}_{cv}(\mathbf{k})a^\dagger_{v,\mathbf{k}}a_{c,\mathbf{k}}\right), \tag{4.8}$$

where $\mathbf{d}_{cv}(\mathbf{k})$ is the dipole moment matrix element

$$\mathbf{d}_{cv}(\mathbf{k}) = \langle c\mathbf{k}|\hat{r}|v\mathbf{k}\rangle, \tag{4.9}$$

and we defined

$$\mathcal{H}_{\mathbf{k}} = \sum_{\ell\ell'}\sum_{\boldsymbol{\delta}_\ell\boldsymbol{\delta}_{\ell'}}h_{\boldsymbol{\delta}_\ell\boldsymbol{\delta}_{\ell'}}(\mathbf{k})b^\dagger_{\mathbf{k}\boldsymbol{\delta}_\ell}b_{\mathbf{k}\boldsymbol{\delta}_{\ell'}}. \tag{4.10}$$

The next step is to calculate the Heisenberg equation of motion

$$-\mathrm{i}\hbar\partial_t\langle\rho_{cv}(\mathbf{k})\rangle = \langle[\mathcal{H},\rho_{cv}(\mathbf{k})]\rangle, \tag{4.11}$$

where $\rho_{cv}(\mathbf{k}) = a^\dagger_{c\mathbf{k}}a_{v\mathbf{k}}$ is the reduced density matrix restricted to the uppermost valence band (v) and lowermost conduction band (c). This is well justified since the transition from v to c is the most likely since it requires less energy, and is commonly referred to as the two-band approximation. Solving Eq. (4.11) involves calculating the commutators of the

right-hand side for each term of the Hamiltonian, which is a lengthy and tedious process that requires repeated applications of the commutation and anticommutation relations of creation and annihilation operators of fermions

$$\{a^{\dagger}_{n_1\mathbf{k}_1}, a_{n_2\mathbf{k}_2}\} = \delta_{n_1 n_2}\delta_{\mathbf{k}_1\mathbf{k}_2}, \tag{4.12a}$$

$$[a_{n_1\mathbf{k}_1}, a_{n_2\mathbf{k}_2}] = [a^{\dagger}_{n_1\mathbf{k}_1}, a^{\dagger}_{n_2\mathbf{k}_2}] = 0. \tag{4.12b}$$

The careful derivation of these commutators are presented in Appendix A. It is important to keep in mind, however, that the full analytical form of these commutators will give rise to an infinity hierarchy problem of n-body operators, $n = 1, 2, 3, \ldots$. To obtain a closed set of equations that can be solved numerically, truncations must be performed. We will follow the approach of Ref. (CHAVES, 2018), that neglects three-body and higher order terms. The resulting equation is

$$\hbar(\omega - \tilde{\omega}_{\mathbf{k}})p_{cv}(\mathbf{k}) + \frac{1}{\mathcal{S}}\sum_{\mathbf{k}'}^{\mathrm{BZ}} K(\mathbf{k},\mathbf{k}')p_{cv}(\mathbf{k}') = \mathbf{d}_{cv}(\mathbf{k})\cdot\boldsymbol{\mathcal{E}}, \tag{4.13}$$

where $p_{cv}(\mathbf{k}) = \langle a^{\dagger}_{c\mathbf{k}}a_{v\mathbf{k}}\rangle$ is the interband transition energy. This is the final form of our SBEs, but some terms must be explicitated. First, the optical band $\tilde{\omega}_{\mathbf{k}}$,

$$\tilde{\omega}_{\mathbf{k}} = E_{c\mathbf{k}} - E_{v\mathbf{k}} + \Sigma_{\mathbf{k}}, \tag{4.14}$$

renormalized to include electron-electron effects through the exchange self-energy

$$\Sigma_{\mathbf{k}} = \frac{1}{\mathcal{S}}\sum_{\ell_1\ell_2}\sum_{\mathbf{G}\mathbf{G}'}\sum_{\mathbf{q}}^{\mathrm{BZ}} \psi^{\ell_1\ell_2}_{\mathbf{G}\mathbf{G}'}(\mathbf{q})[(M^{vv}_{\ell_1}(\mathbf{k},\mathbf{q},\mathbf{G}))^* M^{vv}_{\ell_2}(\mathbf{k},\mathbf{q},\mathbf{G}') + \\ - (M^{cv}_{\ell_1}(\mathbf{k},\mathbf{q},\mathbf{G}))^* M^{vc}_{\ell_2}(\mathbf{k},\mathbf{q},\mathbf{G}')]. \tag{4.15}$$

That is analogous to a G_0W_0 correction. Second, the kernel

$$K(\mathbf{k},\mathbf{k}') = \sum_{\ell_1\ell_2}\sum_{\mathbf{G}\mathbf{G}'} \psi^{\ell_1\ell_2}_{\mathbf{G}\mathbf{G}'}(\mathbf{k}'-\mathbf{k})(M^{cc}_{\ell_1}(\mathbf{k},\mathbf{k}'-\mathbf{k},\mathbf{G}))^* M^{vv}_{\ell_2}(\mathbf{k},\mathbf{k}'-\mathbf{k},\mathbf{G}'), \tag{4.16}$$

which can be thought of, in simple terms, as the term that accounts for the electron-hole Coulomb interactions. At last, the dipole term, which is rewritten as

$$\mathbf{d}_{cv}(\mathbf{k}) = \langle c\mathbf{k}|\hat{r}|v\mathbf{k}\rangle = \frac{\langle c\mathbf{k}|\nabla_{\mathbf{k}}\mathcal{H}_{\mathbf{k}}|v\mathbf{k}\rangle}{E_{c\mathbf{k}} - E_{v\mathbf{k}}}. \tag{4.17}$$

For further information about the derivation of Eqs. (4.13, 4.14, 4.15, 4.16, 4.17), refer to Appendix A.

To evaluate how the excitons are arranged in the material, we evaluate the electron and hole layer compositions for the first 20 bound exciton states. The equations for the probabilities that the electrons and holes of each exciton state are located in the top layer of TBG are

$$\mathcal{P}_{\text{ele}}^{(n)} = \sum_{\mathbf{k}}^{\text{BZ}} \sum_{\boldsymbol{\delta}_2} |u_{c\boldsymbol{\delta}_2}(\mathbf{k}) p_{cv,0}^{(n)}(\mathbf{k})|^2, \tag{4.18a}$$

$$\mathcal{P}_{\text{hol}}^{(n)} = \sum_{\mathbf{k}}^{\text{BZ}} \sum_{\boldsymbol{\delta}_2} |u_{v\boldsymbol{\delta}_2}(\mathbf{k}) p_{cv,0}^{(n)}(\mathbf{k})|^2, \tag{4.18b}$$

where $u_{v\boldsymbol{\delta}_\ell}(\mathbf{k})$ and $u_{c\boldsymbol{\delta}_\ell}(\mathbf{k})$ are the single-particle electron wavefunctions for the highest valence and lowest conduction bands, respectively. Values close to 1 (0) indicate localization of electron or hole in the top (bottom) layer. Values close 0.5, however, will indicate hybridization of the electrons or holes between the layers of the material.

At last, the polarization tensor is derived by means of the Maxwell equations summing all the microscopic electron-hole dipoles, yielding

$$P_{ij}(\omega) = \frac{1}{\mathcal{S}} \sum_{\mathbf{k}}^{\text{BZ}} d_{cv,i}^*(\mathbf{k}) p_{cv,j}(\mathbf{k}), \tag{4.19}$$

where i, j denote the generic components (x of y) of the vector fields $\mathbf{d}_{cv}(\mathbf{k})$ and $\mathbf{p}_{cv}(\mathbf{k})$. The absorption spectrum is defined as the portion of light absorbed by the system through the formation of excitons.

4.3 Results

All reciprocal space calculations of this section were calculated using an auxiliar 2D rectilinear grid, in a similar fashion with the one discussed in Sec. 2.5. When considered useful, the plots are presented for rectangular regions bigger than one reciprocal unit cell.

4.3.1 Optical band

The optical band of TBG, defined as the transition energy between lowest conduction and highest valence bands with a G_0W_0 gap correction, shows interesting 6-fold symmetric patterns. In Fig. 4.1 we present the optical band of TBG for $\theta(1,6) \approx 46.8°$, $V = 3$ eV and $d = 2.8$ Å, showing a profile that resembles a flower of 6 petals. The maximum is localized in the $\mathbf{\Gamma}$ point, and the minima is 6-fold degenerate and localized in the edges of the BZ. We observed that the gap correction $\sum_{\mathbf{k}}$ by itself does not change the overall qualitative behavior of the optical band. However, it dramatically increases the energy

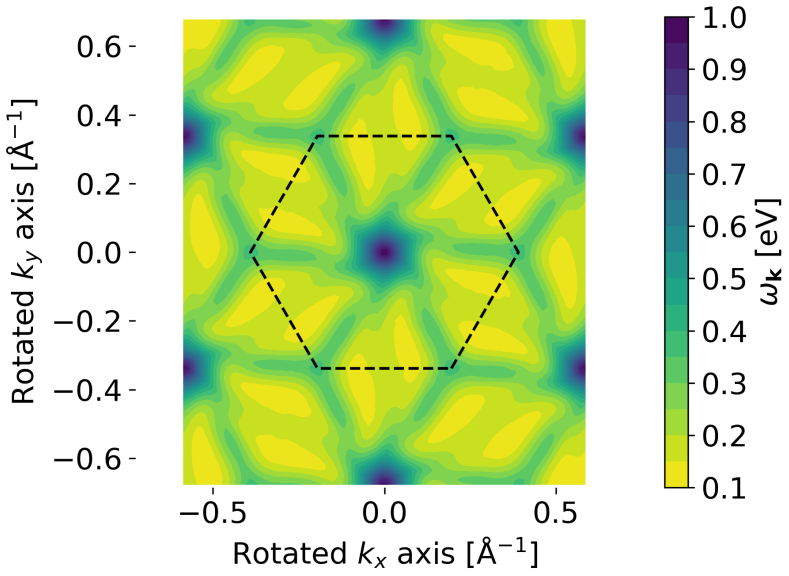

FIGURE 4.1 – (Color online) Optical band (4.14) of TBG for $\theta(1,6) \approx 46.8°$, $V = 3$ eV and $d = 2.8$ Å. The optical bands forms a 6-fold shape, resembling a flower, with 12 degenerate minima located at the edges of the BZ, which is the hexagon contoured using dashed black lines.

gap, corroborating that band gap renormalizations are very significant for the calculation of quasiparticle excitations in 2D materials and must be taken into consideration in order to make accurate predictions.

The optical band minimum convergence was studied as function of the 2D reciprocal rectilinear grid granularity, quantified by a parameter N_y that gives the number of grid points in one direction. The number of points in the remaining perpendicular direction was set to be proportional to N_y and keep the spacing approximately equal in both directions and across the entire grid. As a result, we verified that the convergence of the optical band minimum $\min_{\mathbf{k}} \omega_{\mathbf{k}}$ as a function of $1/N_y$ follows a linear trend, which yields a converged value of $\min_{\mathbf{k}} \omega_{\mathbf{k}} = 135$ meV for $1/N_y \to 0$ ($N_y \to \infty$).

4.3.2 Exciton wavefunctions and binding energies

The exciton wavefunctions $p^{(n)}_{cv,0}(\mathbf{k})$ and energies $\omega^{(n)}_0$ ($n = 1, 2, 3, \ldots$) are obtained by setting the right-hand side of (4.13) to zero and solving it as an eigenvalue problem. All calculations were performed considering TBG for $\theta(1,6) \approx 46.8°$, $V = 3$ eV and $d = 2.8$ Å. In Fig. 4.2 we show the first 80 exciton energies, which are all below the optical gap minimum $\min_{\mathbf{k}} \omega_{\mathbf{k}}$, for a fixed N_y value. Therefore, we observe a rich spectrum of bound excitons, *i.e.*, excitons with energies below the optical band minimum. Here we emphasize that exciton energies and optical band minima must always be compared under the same value of N_y, *i.e.*, exciton energies for a finite N_y value must not be compared with the

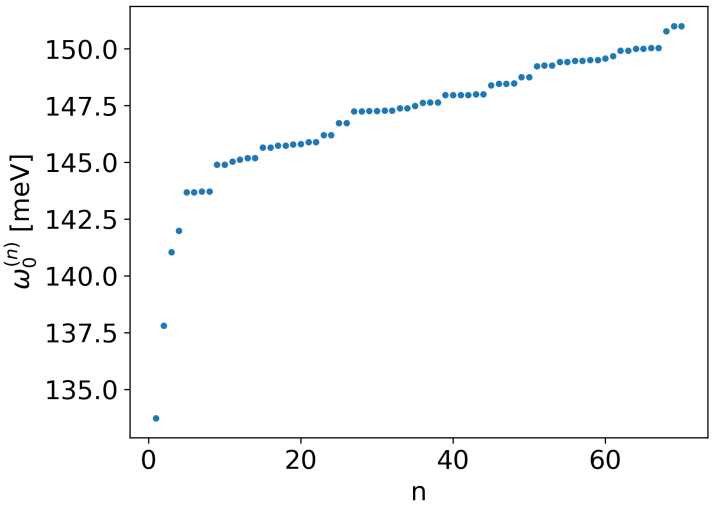

FIGURE 4.2 – (Color online) Spectrum of the exciton energies of TBG for $\theta(1,6) \approx 46.8°$, $V = 3$ eV and $d = 2.8$ Å. We used $N_{\mathbf{k}} = 8600$ sampling $\mathbf{k}$-points (see Eq. 2.32). The first 80 exciton states from the lowest to the highest energy are presented, showing several degenerate sets.

converged optical minimum and *vice-versa*.

The lower exciton wavefunctions must be localized near the most likely formation points in reciprocal space, *i.e.*, the points were the optical band is minimum. Fig. 4.3 presents the lowest exciton wavefunction for a certain N_y value, showing that it forms a dome maximized in a point that corresponds to one of the degenerate optical minima shown in Fig. 4.1. The convergence of this wavefunction was not too harsh, and the dome

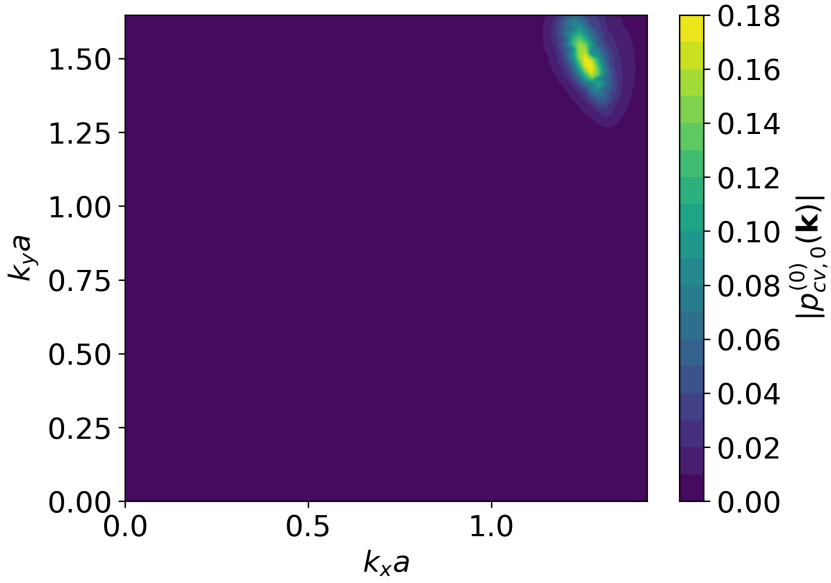

FIGURE 4.3 – (Color online) Wavefunction $p^{(0)}_{cv,0}(\mathbf{k})$ of the lowest exciton of TBG for $\theta(1,6) \approx 46.8°$, $V = 3$ eV and $d = 2.8$ Å, obtained through the solution of the homogeneous SBE, also known as Bethe-Salpeter equation (see Eq. 4.13). The wavefunction presents a stretched dome shape with a peak whose position in momentum space was verified to coincide with one of the minima of the optical band.

manifests strong anisotropy with respect to a pair of perpendicular directions in reciprocal

space.

The convergence of the exciton states must also be considered, with respect to N_y. We performed a convergence study of the lowest exciton energy $\omega_0^{(1)}$ as a function of $1/N_y$, observing that if follows a linear trend. Therefore, we verified that $\omega_0^{(1)} \to 77$ meV when $1/N_y \to 0$ ($N_y \to \infty$). Thus, we obtain a converged binding energy of $\min_{\mathbf{k}} \omega_{\mathbf{k}} - \omega_0^{(1)} = 58$ meV for the lowest exciton, which is an intermediate value in the sense that its much greater than the exciton binding energies found in 3D materials, yet much smaller than the binding energies of 2D semiconductors with greater gaps. This binding energy, however, indicates that TBG can form a rich spectrum of excitons with robust binding energies.

The exciton hybridization between layers was evaluated using the probabilities that electrons and holes are localized in one layer or another (4.18a, 4.18b), as shown in Fig. 4.4. All probabilities are close to 0.5, which denotes a spectrum of bound excitons with

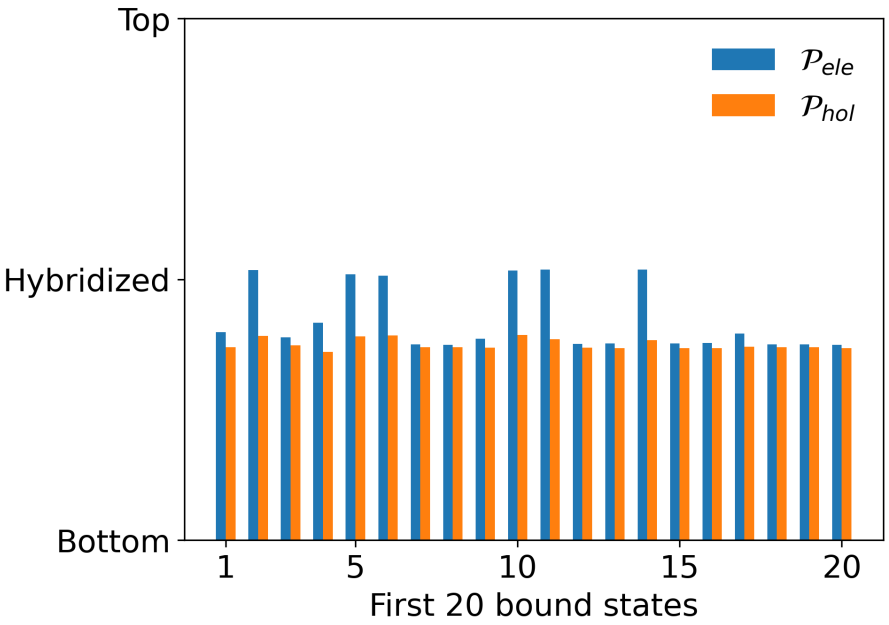

FIGURE 4.4 – (Color online) Bar plot of electron ($\mathcal{P}_{\text{ele}}$) and hole ($\mathcal{P}_{\text{hol}}$) probabilities of being localized in the top or bottom layers (see Eqs. (4.18a, 4.18b)) of TBG, for $\theta(1,6) \approx 46.8°$, $V = 3$ eV and $d = 2.8$ Å. We used $N_{\mathbf{k}} = 8600$ sampling $\mathbf{k}$-points (see Eq. (2.32)). Higher (lower) bars indicate probability values closer to 1 (0). All probabilities are close to 0.5, indicating high exciton hybridization between layers.

strong hybridization between the layers of the material.

4.3.3 Absorption spectrum

The dipole moment was calculated in terms of matrix elements of the gradient of the unperturbed Hamiltonian, as stated in (4.9). The result is present in Fig. (4.5) for our chosen TBG system, showing an interesting 3-fold shape. The brightest regions show the points were the system will interactly more strongly with light, which are all inside the

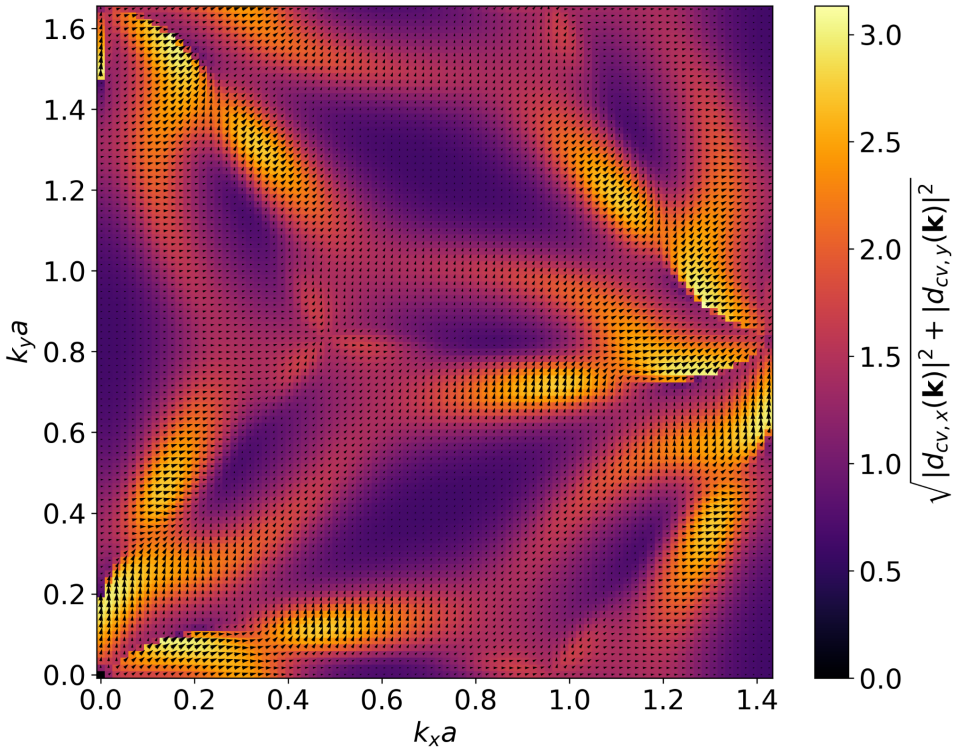

FIGURE 4.5 – (Color online) Dipole moment (4.9) of TBG for $\theta(1,6) \approx 46.8°$, $V = 3$ eV and $d = 2.8$ Å. We used $N_{\mathbf{k}} = 8600$ sampling $\mathbf{k}$-points (see Eq. (2.32)). The arrows indicate the distribution of the dipole moment as a vector field in momentum space. The colormap, on the other hand, displays the magnitude of the dipole moment at each points, such that the brighter regions, where the excitons interact more strongly with light, coincide with the positions where the vector field arrows are bigger. The dipole forms a 3-fold shape, centered at the $\mathbf{K}$ points.

BZ and not localized in any particular high-symmetry point except for $\mathbf{\Gamma}$.

The absorption spectrum is obtained through the polarization tensor (4.19), which by itself is calculated in terms of the interband transition band amplitudes $p_{cv}(\mathbf{k}, \omega)$ that are solutions of (4.13) for a non-vanishing independent term on the right-hand side. Notice that, in this case, (4.13) must be solved as a linear system for a fixed value of ω. The absorption spectrum, presented in Fig. 4.6, shows several peaks, which shows that TBG hosts a rich spectrum of bright excitons, *i.e.*, excitons that can be accessed through light.

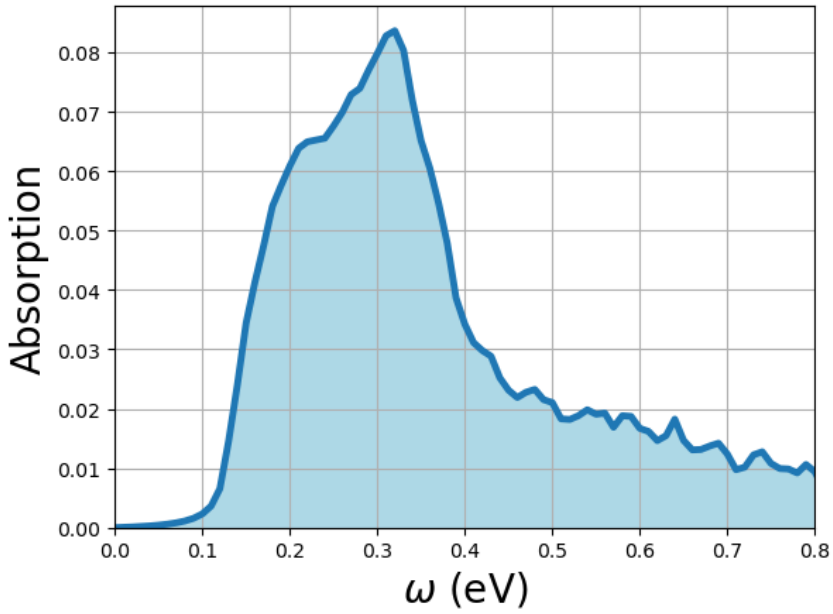

FIGURE 4.6 – (Color online) Absorption spectrum of TBG for $\theta(1,6) \approx 46.8°$, $V = 3$ eV and $d = 2.8$ Å. We used $N_{\mathbf{k}} = 8600$ sampling $\mathbf{k}$-points (see Eq. (2.32)). The spectrum shows a dome-like shape with several peaks. The highest peak is located close to 0.3 eV, and the remaining ones are concentrated to its right. Below 0.1 eV, the absorption is almost zero.

5 Conclusion

In conclusion, we were able to study the low energy physics and exciton formation of TBG. First, in Chapter 2 we applied the tight-binding approximation to model the dominant p_z electrons as a non-interacting gas, which accounts for the effect of the ions of the lattice in the electron system. Through this approach, whose numerical implementation is discussed in greater detail in the previous work (DUARTE, 2022), we were able to model commensurate unit cells of TBG for arbitrary twist angles and reproduce electronic band structure results without the need for geometric relaxation at big angles. Then, we studied the band gap of TBG for all twist angles that generate unit cells with less than 500 atoms as a function of applied vertical bias and pressure. No systematic trend was observed, strongly indicating that the complex lattice of TBG does not have any symmetry protection of the gap. The band gap is opened only for some choices of twist angle, with no particular relation encountered either, and does not surpass 200 meV, which is enough to state that TBG will be a narrow band gap semiconductor when the gap opens, or remain a semi-metal when it does not open. The band gaps for the family of angles $\theta(1, 3k)$, however, exhibit a common qualitative profile, where the maximum value can be achieved with lower pressure by applying the bias.

Next, in Chapter 3 we derived a formalism for the two-body interaction screening in TBG through the dielectric function, which was used both in the context of electron-photon and electron-electron interactions. For the scope of this work, it was sufficient to restrict the dielectric function to the dominant term $\mathbf{G} = \mathbf{G}' = \mathbf{0}$, which exhibits a profile which seems isotropic to the eye with respect to $\mathbf{q}$. The anisotropy, however, is still relevant, and the behavior near $\mathbf{q} = \mathbf{0}$ follows a linear trend as expected, which could be fitted in agreement with the Rytova-Keldysh potential with a ~ 300 Å slope.

Chapter 4 is the most important part of this work, were we used the tools we developed to study exciton formation on TBG under bias and pressure, through the SBE formalism whose foundations are well established. We were able to derive the SBE for a common set of approximations, reaching a final equation which was solved in two ways: first, by setting the independent term to zero and solving the resulting equation as an eigenvalue problem to obtain the excitons energies and wavefunctions; second, by normalizing the electric field of the light and solving the equation as a linear system for fixed values of photon

frequency ω in a range, obtaining the vector field of interband transition amplitudes $\mathbf{p}_{cv}(\mathbf{k}, \omega)$. Through the former, we were able to observe a rich spectrum of bound excitons and a converged binding energy of ~ 60 meV for the lowest exciton. The optical band was calculated with G_0W_0 gap correction was considered in order to obtain more reliable results, showing the formation of 6-fold shape band structures with degenerate minima in the edges of the BZ. With the calculated interband transition amplitudes, we were able to calculate the polarization tensor of the system and, consequently, the absorption spectrum, which showed several peaks indicating that TBG is a potential exciton host platform with a rich spectrum of bright excitons accessible by light.

Bibliography

ADLER, S. L. Quantum theory of the dielectric constant in real solids. **Phys. Rev.**, American Physical Society, v. 126, p. 413–420, Apr 1962. Available at: https://link.aps.org/doi/10.1103/PhysRev.126.413.

AL., E. M. A. et. Resonantly hybridized excitons in moiré superlattices in van der waals heterostructures. Springer Science and Business Media LLC, v. 567, n. 7746, p. 81–86, mar. 2019. Available at: https://doi.org/10.1038/s41586-019-0986-9.

AL., M. C. et. The Chemistry of Two-Dimensional Layered Transition Metal Dichalcogenide Nanosheets. Springer Nature, v. 5, n. 4, p. 263–275, apr 2013. Available at: https://doi.org/10.1038/nchem.1589.

AL., S. M. et. 2D Transition Metal Dichalcogenides. Springer Nature, v. 2, n. 8, p. 17033–17047, jun 2017. Available at: https://www.nature.com/articles/natrevmats201733.pdf.

ANDERSEN, T. I.; SCURI, G.; SUSHKO, A.; GREVE, K. D.; SUNG, J.; ZHOU, Y.; WILD, D. S.; GELLY, R. J.; HEO, H.; BÉRUBÉ, D. *et al.* Excitons in a reconstructed moiré potential in twisted wse 2/wse 2 homobilayers. **Nature Materials**, Nature Publishing Group, v. 20, n. 4, p. 480–487, 2021.

BAEK, H.; BROTONS-GISBERT, M.; KOONG, Z.; CAMPBELL, A.; RAMBACH, M.; WATANABE, K.; TANIGUCHI, T.; GERARDOT, B. Highly energy-tunable quantum light from moiré-trapped excitons. **Science advances**, American Association for the Advancement of Science, v. 6, n. 37, p. eaba8526, 2020.

BAI, Y.; ZHOU, L.; WANG, J.; WU, W.; MCGILLY, L. J.; HALBERTAL, D.; LO, C. F. B.; LIU, F.; ARDELEAN, J.; RIVERA, P. *et al.* Excitons in strain-induced one-dimensional moiré potentials at transition metal dichalcogenide heterojunctions. **Nature Materials**, Nature Publishing Group, v. 19, n. 10, p. 1068–1073, 2020.

BHATTACHARYYA, S.; SINGH, A. K. Semiconductor-metal transition in semiconducting bilayer sheets of transition-metal dichalcogenides. American Physical Society (APS), v. 86, n. 7, p. 075454, ago. 2012. Available at: https://doi.org/10.1103/physrevb.86.075454.

BISTRITZER, R.; MACDONALD, A. H. Moiré bands in twisted double-layer graphene. **Proceedings of the National Academy of Sciences**, National Acad Sciences, v. 108, n. 30, p. 12233–12237, 2011.

BOHM, D.; PINES, D. A collective description of electron interactions. i. magnetic interactions. **Phys. Rev.**, American Physical Society, v. 82, p. 625–634, Jun 1951. Available at: https://link.aps.org/doi/10.1103/PhysRev.82.625.

BOHM, D.; PINES, D. A collective description of electron interactions: Iii. coulomb interactions in a degenerate electron gas. **Phys. Rev.**, American Physical Society, v. 92, p. 609–625, Nov 1953. Available at: https://link.aps.org/doi/10.1103/PhysRev.92.609.

BREM, S.; LIN, K.-Q.; GILLEN, R.; BAUER, J. M.; MAULTZSCH, J.; LUPTON, J. M.; MALIC, E. Hybridized intervalley moiré excitons and flat bands in twisted wse 2 bilayers. **Nanoscale**, Royal Society of Chemistry, v. 12, n. 20, p. 11088–11094, 2020.

CAO, Y.; FATEMI, V.; FANG, S.; WATANABE, K.; TANIGUCHI, T.; KAXIRAS, E.; JARILLO-HERRERO, P. Unconventional superconductivity in magic-angle graphene superlattices. **Nature**, Nature Publishing Group, v. 556, n. 7699, p. 43–50, 2018.

CAO, Y.; LUO, J. Y.; FATEMI, V.; FANG, S.; SANCHEZ-YAMAGISHI, J. D.; WATANABE, K.; TANIGUCHI, T.; KAXIRAS, E.; JARILLO-HERRERO, P. Superlattice-induced insulating states and valley-protected orbits in twisted bilayer graphene. **Phys. Rev. Lett.**, American Physical Society, v. 117, p. 116804, Sep 2016. Available at: https://link.aps.org/doi/10.1103/PhysRevLett.117.116804.

CAO, Y.; RODAN-LEGRAIN, D.; RUBIES-BIGORDA, O.; PARK, J. M.; WATANABE, K.; TANIGUCHI, T.; JARILLO-HERRERO, P. Tunable correlated states and spin-polarized phases in twisted bilayer–bilayer graphene. **Nature**, v. 583, n. 7815, p. 215–220, Jul 2020. ISSN 1476-4687. Available at: https://doi.org/10.1038/s41586-020-2260-6.

CASTRO, E. V.; NOVOSELOV, K. S.; MOROZOV, S. V.; PERES, N. M. R.; SANTOS, J. M. B. L. dos; NILSSON, J.; GUINEA, F.; GEIM, A. K.; NETO, A. H. C. Electronic properties of a biased graphene bilayer. **Journal of Physics: Condensed Matter**, v. 22, n. 17, p. 175503, apr 2010. Available at: https://dx.doi.org/10.1088/0953-8984/22/17/175503.

CEA, T.; GUINEA, F. Band structure and insulating states driven by coulomb interaction in twisted bilayer graphene. **Phys. Rev. B**, American Physical Society, v. 102, p. 045107, Jul 2020. Available at: https://link.aps.org/doi/10.1103/PhysRevB.102.045107.

CHAVES, A. J. **Photonics of graphene and other two-dimensional materials heterostructures**. Monografia (Doutorado) — Departamento de Física, Universidade do Minho, 2018. Available at: https://hdl.handle.net/1822/56302.

CHOI, J.; HSU, W.-T.; LU, L.-S.; SUN, L.; CHENG, H.-Y.; LEE, M.-H.; QUAN, J.; TRAN, K.; WANG, C.-Y.; STAAB, M. *et al.* Moiré potential impedes interlayer exciton diffusion in van der waals heterostructures. **Science advances**, American Association for the Advancement of Science, v. 6, n. 39, p. eaba8866, 2020.

CHOI, Y.; KIM, H.; PENG, Y.; THOMSON, A.; LEWANDOWSKI, C.; POLSKI, R.; ZHANG, Y.; ARORA, H. S.; WATANABE, K.; TANIGUCHI, T.; ALICEA, J.; NADJ-PERGE, S. Correlation-driven topological phases in magic-angle twisted bilayer

graphene. **Nature**, v. 589, n. 7843, p. 536–541, Jan 2021. ISSN 1476-4687. Available at: https://doi.org/10.1038/s41586-020-03159-7.

DAVYDOV, A. S. The theory of molecular excitons. **Soviet Physics Uspekhi**, v. 7, n. 2, p. 145, feb 1964. Available at: https://dx.doi.org/10.1070/PU1964v007n02ABEH003659.

DENG, M.-X.; QI, G. Y.; LUO, W.; MA, R.; WANG, R.-Q.; SHEN, R.; SHENG, L.; XING, D. Y. Superconducting states and majorana modes in transition-metal dichalcogenides under inhomogeneous strain. American Physical Society (APS), v. 99, n. 8, p. 085106, fev. 2019. Available at: https://doi.org/10.1103/physrevb.99.085106.

DONG, L.; LOU, J.; SHENOY, V. B. Large in-plane and vertical piezoelectricity in janus transition metal dichalchogenides. **ACS Nano**, American Chemical Society (ACS), v. 11, n. 8, p. 8242–8248, jul. 2017. Available at: https://doi.org/10.1021/acsnano.7b03313.

DUARTE, V. G. M. **Investigating the effect of twist, electric field and interlayer coupling strength on bilayer graphene**. 61 p. Monografia (Graduação) — Departamento de Engenharia Eletrônica, Instituto Tecnologico de Aeronautica, São Jose dos Campos, 2022. Available at: http://www.bdita.bibl.ita.br/tgsdigitais/lista_resumo-.php?num_tg=78862http://www.bdita.bibl.ita.br/tgsdigitais/lista_resumo.php?num_-tg=78862.

ER, D.; YE, H.; FREY, N. C.; KUMAR, H.; LOU, J.; SHENOY, V. B. Prediction of enhanced catalytic activity for hydrogen evolution reaction in janus transition metal dichalcogenides. ACS Publications, v. 18, n. 6, p. 3943–3949, 2018.

ERKENSTEN, D.; BREM, S.; MALIC, E. Exciton-exciton interaction in transition metal dichalcogenide monolayers and van der waals heterostructures. **Physical Review B**, APS, v. 103, n. 4, p. 045426, 2021.

FÖRG, M.; BAIMURATOV, A. S.; KRUCHININ, S. Y.; VOVK, I. A.; SCHERZER, J.; FÖRSTE, J.; FUNK, V.; WATANABE, K.; TANIGUCHI, T.; HÖGELE, A. Moiré excitons in mose 2-wse 2 heterobilayers and heterotrilayers. **Nature communications**, Nature Publishing Group, v. 12, n. 1, p. 1–7, 2021.

GEIM, A. K. Graphene: Status and prospects. **Science**, v. 324, n. 5934, p. 1530–1534, 2009. Available at: https://www.science.org/doi/abs/10.1126/science.1158877.

GEIM, A. K.; GRIGORIEVA, I. V. Van der waals heterostructures. **Nature**, v. 499, n. 7459, p. 419–425, Jul 2013. ISSN 1476-4687. Available at: https://doi.org/10.1038/nature12385.

HALBERTAL, D.; FINNEY, N. R.; SUNKU, S. S.; KERELSKY, A.; RUBIO-VERDÚ, C.; SHABANI, S.; XIAN, L.; CARR, S.; CHEN, S.; ZHANG, C. *et al.* Moiré metrology of energy landscapes in van der waals heterostructures. **Nature communications**, Nature Publishing Group, v. 12, n. 1, p. 1–8, 2021.

HUANG, K. **Statistical Mechanics**. 2. ed. [*S.l.*]: John Wiley & Sons, 1987.

HUANG, S. e. a. Probing the interlayer coupling of twisted bilayer MoS_2 using photoluminescence spectroscopy. ACS Publications, v. 14, n. 10, p. 5500–5508, 2014.

KANG, J.; AL. et. Electronic structural moiré pattern effects on $MoS_2/MoSe_2$ 2D heterostructures. ACS Publications, v. 13, n. 11, p. 5485–5490, 2013.

KELDYSH, L. V. Coulomb interaction in thin semiconductor and semimetal films. **JETP Lett.**, v. 658, n. 29, 1979.

KERELSKY, A.; MCGILLY, L. J.; KENNES, D. M.; XIAN, L.; YANKOWITZ, M.; CHEN, S.; WATANABE, K.; TANIGUCHI, T.; HONE, J.; DEAN, C.; RUBIO, A.; PASUPATHY, A. N. Maximized electron interactions at the magic angle in twisted bilayer graphene. **Nature**, v. 572, n. 7767, p. 95–100, Aug 2019. ISSN 1476-4687. Available at: https://doi.org/10.1038/s41586-019-1431-9.

KIRA, M.; KOCH, S. W. **Semiconductor Quantum Optics**. [*S.l.*]: Cambridge University Press, 2011.

KRETSCHMER, S.; KOMSA, H.-P.; BØGGILD, P.; KRASHENINNIKOV, A. V. Structural transformations in two-dimensional transition-metal dichalcogenide MoS_2 under an electron beam: Insights from first-principles calculations. American Chemical Society (ACS), v. 8, n. 13, p. 3061–3067, jun 2017. Available at: https://doi.org/10.1021/acs.jpclett.7b01177.

LI, E.; WANG, D.; FAN, P.; ZHANG, R.; ZHANG, Y.-Y.; LI, G.; MAO, J.; WANG, Y.; LIN, X.; DU, S.; GAO, H.-J. Construction of bilayer $PdSe_2$ on epitaxial graphene. Springer Science and Business Media LLC, v. 11, n. 11, p. 5858–5865, maio 2018. Available at: https://doi.org/10.1007/s12274-018-2090-0.

LI, F.; WEI, W.; ZHAO, P.; HUANG, B.; DAI, Y. Electronic and optical properties of pristine and vertical and lateral heterostructures of janus MoSSe and WSSe. ACS Publications, v. 8, n. 23, p. 5959–5965, 2017.

LI, G.; LUICAN, A.; SANTOS, J. L. D.; NETO, A. C.; REINA, A.; KONG, J.; ANDREI, E. Observation of van hove singularities in twisted graphene layers. **Nature Physics**, Nature Publishing Group, v. 6, n. 2, p. 109–113, 2010.

LI, W.; LU, X.; DUBEY, S.; DEVENICA, L.; SRIVASTAVA, A. Dipolar interactions between localized interlayer excitons in van der waals heterostructures. **Nature materials**, Nature Publishing Group, v. 19, n. 6, p. 624–629, 2020.

LIN, M.-L. e. a. Moiré phonons in twisted bilayer MoS_2. ACS Publications, v. 12, n. 8, p. 8770–8780, 2018.

LING, X.; WANG, H.; HUANG, S.; XIA, F.; DRESSELHAUS, M. S. The renaissance of black phosphorus. **Proceedings of the National Academy of Sciences**, v. 112, n. 15, p. 4523–4530, 2015. Available at: https://www.pnas.org/doi/abs/10.1073/pnas.1416581112.

LONG, C.; DAI, Y.; GONG, Z.-R.; JIN, H. Robust type-II band alignment in janus-MoSSe bilayer with extremely long carrier lifetime induced by the intrinsic electric field. American Physical Society (APS), v. 99, n. 11, p. 115316, mar. 2019. Available at: https://doi.org/10.1103/physrevb.99.115316.

LU, A.-Y.; AL. et. Janus monolayers of transition metal dichalcogenides. Springer Science and Business Media LLC, v. 12, n. 8, p. 744–749, maio 2017. Available at: https://doi.org/10.1038/nnano.2017.100.

LUCATTO, B.; KODA, D. S.; BECHSTEDT, F.; MARQUES, M.; TELES, L. K. Charge qubit in van der waals heterostructures. **Phys. Rev. B**, American Physical Society, v. 100, p. 121406, Sep 2019. Available at: https://link.aps.org/doi/10.1103/PhysRevB.100.121406.

MANZELI, S.; OVCHINNIKOV, D.; PASQUIER, D.; YAZYEV, O. V.; KIS, A. 2d transition metal dichalcogenides. **Nature Reviews Materials**, v. 2, n. 8, p. 17033, Jun 2017. ISSN 2058-8437. Available at: https://doi.org/10.1038/natrevmats.2017.33.

MARAGKOU, M. The dark exciton as a qubit. **Nature Materials**, v. 14, n. 3, p. 260–260, Mar 2015. ISSN 1476-4660. Available at: https://doi.org/10.1038/nmat4243.

MARDER, M. **Condensed Matter Physics**. Wiley, 2010. ISBN 9780470949948. Available at: https://books.google.com.br/books?id=ijloadAt4BQC.

MELE, E. J. Commensuration and interlayer coherence in twisted bilayer graphene. **Phys. Rev. B**, American Physical Society, v. 81, p. 161405, Apr 2010. Available at: https://link.aps.org/doi/10.1103/PhysRevB.81.161405.

MERKL, P.; MOOSHAMMER, F.; BREM, S.; GIRNGHUBER, A.; LIN, K.-Q.; WEIGL, L.; LIEBICH, M.; YONG, C.-K.; GILLEN, R.; MAULTZSCH, J. *et al.* Twist-tailoring coulomb correlations in van der waals homobilayers. **Nature communications**, Nature Publishing Group, v. 11, n. 1, p. 1–7, 2020.

MIRZAKHANI, M.; PEETERS, F. M.; ZARENIA, M. Circular quantum dots in twisted bilayer graphene. **Phys. Rev. B**, American Physical Society, v. 101, p. 075413, Feb 2020. Available at: https://link.aps.org/doi/10.1103/PhysRevB.101.075413.

MOON, P.; KOSHINO, M. Optical absorption in twisted bilayer graphene. **Phys. Rev. B**, American Physical Society, v. 87, p. 205404, May 2013. Available at: https://link.aps.org/doi/10.1103/PhysRevB.87.205404.

MORELL, E. S.; CORREA, J. D.; VARGAS, P.; PACHECO, M.; BARTICEVIC, Z. Flat bands in slightly twisted bilayer graphene: Tight-binding calculations. **Phys. Rev. B**, American Physical Society, v. 82, p. 121407, Sep 2010. Available at: https://link.aps.org/doi/10.1103/PhysRevB.82.121407.

NAIK, M. H.; JAIN, M. Ultraflatbands and shear solitons in moire patterns of twisted bilayer transition metal dichalcogenides. APS, v. 121, n. 26, p. 266401, 2018.

NAIK, M. H.; MAITY, I.; MAITI, P. K.; JAIN, M. Kolmogorov–crespi potential for multilayer transition-metal dichalcogenides: Capturing structural transformations in moiré superlattices. ACS Publications, v. 123, n. 15, p. 9770–9778, 2019.

NETO, A. H. C.; GUINEA, F.; PERES, N. M. R.; NOVOSELOV, K. S.; GEIM, A. K. The electronic properties of graphene. **Rev. Mod. Phys.**, American Physical Society, v. 81, p. 109–162, Jan 2009. Available at: https://link.aps.org/doi/10.1103/RevModPhys.81.109.

PARK, M. J.; KIM, Y.; CHO, G. Y.; LEE, S. Higher-order topological insulator in twisted bilayer graphene. **Phys. Rev. Lett.**, American Physical Society, v. 123, p. 216803, Nov 2019. Available at: https://link.aps.org/doi/10.1103/PhysRevLett.123.216803.

PENG, R.; MA, Y.; HUANG, B.; DAI, Y. Two-dimensional janus PtSSe for photocatalytic water splitting under the visible or infrared light. Royal Society of Chemistry (RSC), v. 7, n. 2, p. 603–610, 2019. Available at: https://doi.org/10.1039/c8ta09177c.

PINES, D.; BOHM, D. A collective description of electron interactions: Ii. collective vs individual particle aspects of the interactions. **Phys. Rev.**, American Physical Society, v. 85, p. 338–353, Jan 1952. Available at: https://link.aps.org/doi/10.1103/PhysRev.85.338.

POLINI, M.; TOMADIN, A.; ASGARI, R.; MACDONALD, A. H. Density functional theory of graphene sheets. **Phys. Rev. B**, American Physical Society, v. 78, p. 115426, Sep 2008. Available at: https://link.aps.org/doi/10.1103/PhysRevB.78.115426.

POLSHYN, H.; YANKOWITZ, M.; CHEN, S.; ZHANG, Y.; WATANABE, K.; TANIGUCHI, T.; DEAN, C. R.; YOUNG, A. F. Large linear-in-temperature resistivity in twisted bilayer graphene. **Nature Physics**, v. 15, n. 10, p. 1011–1016, Oct 2019. ISSN 1745-2481. Available at: https://doi.org/10.1038/s41567-019-0596-3.

ROSENBERGER, M. R.; CHUANG, H.-J.; PHILLIPS, M.; OLESHKO, V. P.; MCCREARY, K. M.; SIVARAM, S. V.; HELLBERG, C. S.; JONKER, B. T. Twist angle-dependent atomic reconstruction and moiré patterns in transition metal dichalcogenide heterostructures. **ACS nano**, ACS Publications, v. 14, n. 4, p. 4550–4558, 2020.

RYTOVA, N. S. Screened potential of a point charge in a thin film. **Phys. Astron.**, Proc. Moscow State University, v. 30, n. 3, 1967.

SANTOS, J. M. B. Lopes dos; PERES, N. M. R.; NETO, A. H. C. Graphene bilayer with a twist: Electronic structure. **Phys. Rev. Lett.**, American Physical Society, v. 99, p. 256802, Dec 2007. Available at: https://link.aps.org/doi/10.1103/PhysRevLett.99.256802.

SANTOS, J. M. B. Lopes dos; PERES, N. M. R.; NETO, A. H. C. Continuum model of the twisted graphene bilayer. **Phys. Rev. B**, American Physical Society, v. 86, p. 155449, Oct 2012. Available at: https://link.aps.org/doi/10.1103/PhysRevB.86.155449.

SHABANI, S.; HALBERTAL, D.; WU, W.; CHEN, M.; LIU, S.; HONE, J.; YAO, W.; BASOV, D. N.; ZHU, X.; PASUPATHY, A. N. Deep moiré potentials in twisted transition metal dichalcogenide bilayers. **Nature Physics**, Nature Publishing Group, p. 1–6, 2021.

SHALLCROSS, S.; SHARMA, S.; KANDELAKI, E.; PANKRATOV, O. A. Electronic structure of turbostratic graphene. **Phys. Rev. B**, American Physical Society, v. 81, p. 165105, Apr 2010. Available at: https://link.aps.org/doi/10.1103/PhysRevB.81.165105.

SHARMA, M.; KUMAR, A.; AHLUWALIA, P. K.; PANDEY, R. Strain and electric field induced electronic properties of two-dimensional hybrid bilayers of transition-metal dichalcogenides. AIP Publishing, v. 116, n. 6, p. 063711, ago. 2014. Available at: https://doi.org/10.1063/1.4892798.

SHIMAZAKI, Y.; SCHWARTZ, I.; WATANABE, K.; TANIGUCHI, T.; KRONER, M.; IMAMOĞLU, A. Strongly correlated electrons and hybrid excitons in a moiré heterostructure. **Nature**, Nature Publishing Group, v. 580, n. 7804, p. 472–477, 2020.

SLATER, J. C.; KOSTER, G. F. Simplified lcao method for the periodic potential problem. **Phys. Rev.**, American Physical Society, v. 94, p. 1498–1524, Jun 1954. Available at: https://link.aps.org/doi/10.1103/PhysRev.94.1498.

SONG, Z.; WANG, Z.; SHI, W.; LI, G.; FANG, C.; BERNEVIG, B. A. All magic angles in twisted bilayer graphene are topological. **Phys. Rev. Lett.**, American Physical Society, v. 123, p. 036401, Jul 2019. Available at: https://link.aps.org/doi/10.1103/PhysRevLett.123.036401.

TANG, Y.; GU, J.; LIU, S.; WATANABE, K.; TANIGUCHI, T.; HONE, J.; MAK, K. F.; SHAN, J. Tuning layer-hybridized moiré excitons by the quantum-confined stark effect. **Nature Nanotechnology**, Nature Publishing Group, v. 16, n. 1, p. 52–57, 2021.

WISER, N. Dielectric constant with local field effects included. **Phys. Rev.**, American Physical Society, v. 129, p. 62–69, Jan 1963. Available at: https://link.aps.org/doi/10.1103/PhysRev.129.62.

XIE, M.; MACDONALD, A. H. Nature of the correlated insulator states in twisted bilayer graphene. **Phys. Rev. Lett.**, American Physical Society, v. 124, p. 097601, Mar 2020. Available at: https://link.aps.org/doi/10.1103/PhysRevLett.124.097601.

XU, Y.; HORN, C.; ZHU, J.; TANG, Y.; MA, L.; LI, L.; LIU, S.; WATANABE, K.; TANIGUCHI, T.; HONE, J. C. *et al.* Creation of moiré bands in a monolayer semiconductor by spatially periodic dielectric screening. **Nature Materials**, Nature Publishing Group, p. 1–5, 2021.

YIN, W.-J.; WEN, B.; NIE, G.-Z.; WEI, X.-L.; LIU, L.-M. Tunable dipole and carrier mobility for a few layer janus MoSSe structure. Royal Society of Chemistry, v. 6, n. 7, p. 1693–1700, 2018.

ZANDE, A. M. van D.; AL. et. Tailoring the electronic structure in bilayer molybdenum disulfide via interlayer twist. ACS Publications, v. 14, n. 7, p. 3869–3875, 2014.

ZENG, L.-H.; WU, D.; LIN, S.-H.; XIE, C.; YUAN, H.-Y.; LU, W.; LAU, S. P.; CHAI, Y.; LUO, L.-B.; LI, Z.-J.; TSANG, Y. H. Controlled synthesis of 2D palladium diselenide for sensitive photodetector applications. Wiley, v. 29, n. 1, p. 1806878, nov. 2018. Available at: https://doi.org/10.1002/adfm.201806878.

ZHANG, J.; AL. et. Janus monolayer transition-metal dichalcogenides. ACS Publications, v. 11, n. 8, p. 8192–8198, 2017.

ZHANG, K.; FENG, Y.; WANG, F.; YANG, Z.; WANG, J. Two dimensional hexagonal boron nitride (2d-hbn): synthesis, properties and applications. **J. Mater. Chem. C**, The

Royal Society of Chemistry, v. 5, p. 11992–12022, 2017. Available at: http://dx.doi.org/10.1039/C7TC04300Ghttp://dx.doi.org/10.1039/C7TC04300G.

ZHANG, L.; ZHANG, Z.; WU, F.; WANG, D.; GOGNA, R.; HOU, S.; WATANABE, K.; TANIGUCHI, T.; KULKARNI, K.; KUO, T. *et al.* Twist-angle dependence of moiré excitons in ws 2/mose 2 heterobilayers. **Nature communications**, Nature Publishing Group, v. 11, n. 1, p. 1–8, 2020.

ZHAO, D.; XIE, S.; WANG, Y.; ZHU, H.; CHEN, L.; SUN, Q.; ZHANG, D. W. Synthesis of large-scale few-layer PtS2 films by chemical vapor deposition. AIP Publishing, v. 9, n. 2, p. 025225, fev. 2019. Available at: https://doi.org/10.1063/1.5086447.

Appendix A - Detailed derivation of the Semiconductor Bloch Equations

In this Appendix we present a possible way of deriving the Semiconductor Bloch Equations (SBE). It is analogous to what is presented in Section 4.2, but there we also showed how to obtain the SBE by particularizing the procedure of Ref. (CHAVES, 2018), which considers a more general case.

The derivation of the SBE starts from the Heisenberg equation of motion

$$-\mathrm{i}\hbar\partial_t\langle\rho_{cv}(\mathbf{k})\rangle = \langle[\mathcal{H}, \rho_{cv}(\mathbf{k})]\rangle. \tag{A.1}$$

Using $\rho_{cv}(\mathbf{k}) = a^\dagger_{c\mathbf{k}}a_{v\mathbf{k}}$ and $\mathcal{H} = \mathcal{H}_0 + \mathcal{H}_I + \mathcal{H}_{ee}$, we expand the commutator of the right-hand side of (A.1):

$$[\mathcal{H}, \rho_{cv}(\mathbf{k})] = [\mathcal{H}_0, a^\dagger_{c\mathbf{k}}a_{v\mathbf{k}}] + [\mathcal{H}_I, a^\dagger_{c\mathbf{k}}a_{v\mathbf{k}}] + [\mathcal{H}_{ee}, a^\dagger_{c\mathbf{k}}a_{v\mathbf{k}}]. \tag{A.2}$$

Each term of this equation shall be explicitated carefully, taking the commutation and anticommutation rules of fermionic operators into account:

$$\{a^\dagger_{n\mathbf{k}}, a_{n'\mathbf{k}'}\} = \delta_{nn'}\delta_{\mathbf{k}\mathbf{k}'}, \tag{A.3a}$$

$$[a_{n\mathbf{k}}, a_{n'\mathbf{k}'}] = [a^\dagger_{n\mathbf{k}}, a^\dagger_{n'\mathbf{k}'}] = 0. \tag{A.3b}$$

We begin with the single-particle tight-binding Hamiltonian (2.29b):

$$[\mathcal{H}_0, a^\dagger_{c\mathbf{k}}a_{v\mathbf{k}}] = \sum_n \sum_{\mathbf{k}'}^{\mathrm{BZ}} E_{n\mathbf{k}'}[a^\dagger_{n\mathbf{k}'}a_{n\mathbf{k}'}, a^\dagger_{c\mathbf{k}}a_{v\mathbf{k}}] \tag{A.4a}$$

$$= \sum_n \sum_{\mathbf{k}'}^{\mathrm{BZ}} E_{n\mathbf{k}'}\left[a^\dagger_{n\mathbf{k}'}(\delta_{nc}\delta_{\mathbf{k}\mathbf{k}'} - a^\dagger_{c\mathbf{k}}a_{n\mathbf{k}'})a_{v\mathbf{k}} - a^\dagger_{c\mathbf{k}}(\delta_{nv}\delta_{\mathbf{k}\mathbf{k}'} - a^\dagger_{n\mathbf{k}'}a_{v\mathbf{k}})a_{n\mathbf{k}'}\right] \tag{A.4b}$$

$$= (E_{c\mathbf{k}} - E_{v\mathbf{k}})a^\dagger_{c\mathbf{k}}a_{v\mathbf{k}}. \tag{A.4c}$$

This term represents the optical band without any gap correction. Next, we look into the dipole energy term (4.8):

$$[\mathcal{H}_I, a^\dagger_{c\mathbf{k}} a_{v\mathbf{k}}] = -\sum_{\mathbf{k}'}^{\mathrm{BZ}} \boldsymbol{\mathcal{E}} \cdot \mathbf{d}^*_{cv}(\mathbf{k}')[a^\dagger_{c\mathbf{k}'} a_{v\mathbf{k}'}, a^\dagger_{c\mathbf{k}} a_{v\mathbf{k}}] + \boldsymbol{\mathcal{E}} \cdot \mathbf{d}_{cv}(\mathbf{k}')[a^\dagger_{v\mathbf{k}'} a_{c\mathbf{k}'}, a^\dagger_{c\mathbf{k}} a_{v\mathbf{k}}] \tag{A.5a}$$

$$\begin{aligned} &= -\sum_{\mathbf{k}'}^{\mathrm{BZ}} \boldsymbol{\mathcal{E}} \cdot \mathbf{d}^*_{cv}(\mathbf{k}') \left[a^\dagger_{c\mathbf{k}'}(-a^\dagger_{c\mathbf{k}} a_{v\mathbf{k}'}) a_{v\mathbf{k}} - a^\dagger_{c\mathbf{k}}(-a^\dagger_{c\mathbf{k}'} a_{v\mathbf{k}}) a_{v\mathbf{k}'} \right] + \\ &+ \boldsymbol{\mathcal{E}} \cdot \mathbf{d}_{cv}(\mathbf{k}') \left[a^\dagger_{v\mathbf{k}'}(\delta_{\mathbf{k}\mathbf{k}'} - a^\dagger_{c\mathbf{k}} a_{c\mathbf{k}'}) a_{v\mathbf{k}} - a^\dagger_{c\mathbf{k}}(\delta_{\mathbf{k}\mathbf{k}'} - a^\dagger_{v\mathbf{k}'} a_{v\mathbf{k}}) a_{c\mathbf{k}'} \right] \end{aligned} \tag{A.5b}$$

$$= \boldsymbol{\mathcal{E}} \cdot \mathbf{d}_{cv}(\mathbf{k})(a^\dagger_{c\mathbf{k}} a_{c\mathbf{k}} - a^\dagger_{v\mathbf{k}} a_{v\mathbf{k}}). \tag{A.5c}$$

This first two terms are both single-particle ones, where the simplification is fairly straightforward. The last term, on the other hand, will be handled separately since it describes two-particle interactions and will require much more algebraic dexterity.

The electron-electron interaction commutator is expanded substituting (4.6b):

$$\begin{aligned} [\mathcal{H}_{ee}, a^\dagger_{c\mathbf{k}} a_{v\mathbf{k}}] = -\frac{e}{2S} \sum_{\ell_1 \ell_2} \sum_{n_1 n_2 n_3 n_4} \sum_{\mathbf{k}_1 \mathbf{k}_2}^{\mathrm{BZ}} \sum_{\mathbf{q}} \sum_{\mathbf{G}\mathbf{G}'} \psi^{\ell_1 \ell_2}_{\mathbf{G}\mathbf{G}'}(\mathbf{q}) \times \\ \times [M^{n_1 n_4}_{\ell_1}(\mathbf{k}_1, \mathbf{q}, \mathbf{G}')]^* M^{n_2 n_3}_{\ell_2}(\mathbf{k}_2, \mathbf{q}, \mathbf{G}) [a^\dagger_{n_1, \mathbf{k}_1 + \mathbf{q}} a^\dagger_{n_2 \mathbf{k}_2} a_{n_3, \mathbf{k}_2 + \mathbf{q}} a_{n_4 \mathbf{k}_1}, a^\dagger_{c\mathbf{k}} a_{v\mathbf{k}}]. \end{aligned} \tag{A.6}$$

Now we expand the commutator on the right-hand side

$$\begin{aligned} [a^\dagger_{n_1, \mathbf{k}_1 + \mathbf{q}} a^\dagger_{n_2 \mathbf{k}_2} a_{n_3, \mathbf{k}_2 + \mathbf{q}} a_{n_4 \mathbf{k}_1}, a^\dagger_{c\mathbf{k}} a_{v\mathbf{k}}] = \\ a^\dagger_{n_1, \mathbf{k}_1 + \mathbf{q}} a^\dagger_{n_2 \mathbf{k}_2} a_{n_3, \mathbf{k}_2 + \mathbf{q}} (\delta_{n_4 c} \delta_{\mathbf{k}\mathbf{k}_1} - a^\dagger_{c\mathbf{k}} a_{n_4 \mathbf{k}_1}) a_{v\mathbf{k}} + \\ - a^\dagger_{c\mathbf{k}} (\delta_{n_1 v} \delta_{\mathbf{k}, \mathbf{k}_1 + \mathbf{q}} - a^\dagger_{n_1, \mathbf{k}_1 + \mathbf{q}} a_{v\mathbf{k}}) a^\dagger_{n_2 \mathbf{k}_2} a_{n_3, \mathbf{k}_2 + \mathbf{q}} a_{n_4 \mathbf{k}_4} \end{aligned} \tag{A.7a}$$

$$\begin{aligned} = \delta_{n_4 c} \delta_{\mathbf{k}\mathbf{k}_1} a^\dagger_{n_1, \mathbf{k}_1 + \mathbf{q}} a^\dagger_{n_2 \mathbf{k}_2} a_{n_3, \mathbf{k}_2 + \mathbf{q}} a_{v\mathbf{k}} - a^\dagger_{n_1, \mathbf{k}_1 + \mathbf{q}} a^\dagger_{n_2 \mathbf{k}_2} a_{n_3, \mathbf{k}_2 + \mathbf{q}} a^\dagger_{c\mathbf{k}} a_{n_4 \mathbf{k}_1} a_{v\mathbf{k}} + \\ - \delta_{n_1 v} \delta_{\mathbf{k}, \mathbf{k}_1 + \mathbf{q}} a^\dagger_{c\mathbf{k}} a^\dagger_{n_2 \mathbf{k}_2} a_{n_3, \mathbf{k}_2 + \mathbf{q}} a_{n_4 \mathbf{k}_4} + a^\dagger_{c\mathbf{k}} a^\dagger_{n_1, \mathbf{k}_1 + \mathbf{q}} a_{v\mathbf{k}} a^\dagger_{n_2 \mathbf{k}_2} a_{n_3, \mathbf{k}_2 + \mathbf{q}} a_{n_4 \mathbf{k}_4}. \end{aligned} \tag{A.7b}$$

The second and fourth term on the right-hand side of the equation above can be gathered and simplified as

$$\begin{aligned} - a^\dagger_{n_1, \mathbf{k}_1 + \mathbf{q}} a^\dagger_{n_2 \mathbf{k}_2} a_{n_3, \mathbf{k}_2 + \mathbf{q}} a^\dagger_{c\mathbf{k}} a_{n_4 \mathbf{k}_1} a_{v\mathbf{k}} + a^\dagger_{c\mathbf{k}} a^\dagger_{n_1, \mathbf{k}_1 + \mathbf{q}} a_{v\mathbf{k}} a^\dagger_{n_2 \mathbf{k}_2} a_{n_3, \mathbf{k}_2 + \mathbf{q}} a_{n_4 \mathbf{k}_4} = \\ = -a^\dagger_{n_1, \mathbf{k}_1 + \mathbf{q}} a^\dagger_{n_2 \mathbf{k}_2} (\delta_{n_3 c} \delta_{\mathbf{k}, \mathbf{k}_2 + \mathbf{q}} - a^\dagger_{c\mathbf{k}} a_{n_3, \mathbf{k}_2 + \mathbf{q}}) a_{n_4 \mathbf{k}_1} a_{v\mathbf{k}} + \\ + a^\dagger_{c\mathbf{k}} a^\dagger_{n_1, \mathbf{k}_1 + \mathbf{q}} (\delta_{n_2 v} \delta_{\mathbf{k}\mathbf{k}_2} - a^\dagger_{n_2 \mathbf{k}_2} a_{v\mathbf{k}}) a_{n_3, \mathbf{k}_2 + \mathbf{q}} a_{n_4 \mathbf{k}_1} \end{aligned} \tag{A.8a}$$

$$= \quad -\delta_{n_3c}\delta_{\mathbf{k},\mathbf{k}_2+\mathbf{q}}a^\dagger_{n_1,\mathbf{k}_1+\mathbf{q}}a^\dagger_{n_2\mathbf{k}_2}a_{n_4\mathbf{k}_1}a_{v\mathbf{k}} \;+\; \delta_{n_2v}\delta_{\mathbf{k}\mathbf{k}_2}a^\dagger_{c\mathbf{k}}a^\dagger_{n_1,\mathbf{k}_1+\mathbf{q}}a_{n_3,\mathbf{k}_2+\mathbf{q}}a_{n_4\mathbf{k}_1}. \quad \text{(A.8b)}$$

Substituting (A.8b) back on (A.7b), we get

$$\begin{aligned}[a^\dagger_{n_1,\mathbf{k}_1+\mathbf{q}}a^\dagger_{n_2\mathbf{k}_2}a_{n_3,\mathbf{k}_2+\mathbf{q}}a_{n_4\mathbf{k}_1}, a^\dagger_{c\mathbf{k}}a_{v\mathbf{k}}] &= \delta_{n_4c}\delta_{\mathbf{k}\mathbf{k}_1}a^\dagger_{n_1,\mathbf{k}_1+\mathbf{q}}a^\dagger_{n_2\mathbf{k}_2}a_{n_3,\mathbf{k}_2+\mathbf{q}}a_{v\mathbf{k}}+\\ &- \delta_{n_3c}\delta_{\mathbf{k},\mathbf{k}_2+\mathbf{q}}a^\dagger_{n_1,\mathbf{k}_1+\mathbf{q}}a^\dagger_{n_2\mathbf{k}_2}a_{n_4\mathbf{k}_1}a_{v\mathbf{k}} - \delta_{n_1v}\delta_{\mathbf{k},\mathbf{k}_1+\mathbf{q}}a^\dagger_{c\mathbf{k}}a^\dagger_{n_2\mathbf{k}_2}a_{n_3,\mathbf{k}_2+\mathbf{q}}a_{n_4\mathbf{k}_4}+\\ &+ \delta_{n_2v}\delta_{\mathbf{k}\mathbf{k}_2}a^\dagger_{c\mathbf{k}}a^\dagger_{n_1,\mathbf{k}_1+\mathbf{q}}a_{n_3,\mathbf{k}_2+\mathbf{q}}a_{n_4\mathbf{k}_1}, \quad \text{(A.9)}\end{aligned}$$

which allows us to simplify (A.6), exchanging some summation indices for tidiness:

$$\begin{aligned}[\mathcal{H}_{ee}, a^\dagger_{c\mathbf{k}}a_{v\mathbf{k}}] = -\frac{e}{2\mathcal{S}}\sum_{\ell_1\ell_2}\sum_{\boldsymbol{\delta}_{\ell_1}\boldsymbol{\delta}_{\ell_2}}\sum_{n_1n_2n_3}\sum_{\mathbf{k}_1}\sum_{\mathbf{q}}^{\mathrm{BZ}}\sum_{\mathbf{G}\mathbf{G}'}\psi^{\ell_1\ell_2}_{\mathbf{G}\mathbf{G}'}(\mathbf{q})\times\\ \times\Big\{[M^{n_1c}_{\ell_1}(\mathbf{k},\mathbf{q},\mathbf{G}')]^*M^{n_2n_3}_{\ell_2}(\mathbf{k}_1,\mathbf{q},\mathbf{G})a^\dagger_{n_1,\mathbf{k}+\mathbf{q}}a^\dagger_{n_2\mathbf{k}_1}a_{n_3,\mathbf{k}_1+\mathbf{q}}a_{v\mathbf{k}}+\\ -[M^{vn_1}_{\ell_1}(\mathbf{k}-\mathbf{q},\mathbf{q},\mathbf{G}')]^*M^{n_2n_3}_{\ell_2}(\mathbf{k}_1,\mathbf{q},\mathbf{G})a^\dagger_{c\mathbf{k}}a^\dagger_{n_2\mathbf{k}_1}a_{n_3,\mathbf{k}_1+\mathbf{q}}a_{n_1,\mathbf{k}-\mathbf{q}}+\\ -[M^{n_1n_3}_{\ell_1}(\mathbf{k}_1,\mathbf{q},\mathbf{G}')]^*M^{n_2c}_{\ell_2}(\mathbf{k}-\mathbf{q},\mathbf{q},\mathbf{G})a^\dagger_{n_1,\mathbf{k}_1+\mathbf{q}}a^\dagger_{n_2,\mathbf{k}-\mathbf{q}}a_{n_3\mathbf{k}_1}a_{v\mathbf{k}}+\\ +[M^{n_1n_2}_{\ell_1}(\mathbf{k}_1,\mathbf{q},\mathbf{G}')]^*M^{vn_3}_{\ell_2}(\mathbf{k},\mathbf{q},\mathbf{G})a^\dagger_{c\mathbf{k}}a^\dagger_{n_1,\mathbf{k}_1+\mathbf{q}}a_{n_3,\mathbf{k}+\mathbf{q}}a_{n_2\mathbf{k}_1}\Big\}. \quad \text{(A.10)}\end{aligned}$$

For the purposes of this work, we restrict each term in (A.10) to interband transitions between the uppermost valence band (v) and the lowermost conduction band (c), which allow us simplify the electron-electron interaction commutator to

$$\begin{aligned}[\mathcal{H}_{ee}, a^\dagger_{c\mathbf{k}}a_{v\mathbf{k}}] = -\frac{e}{2\mathcal{S}}\sum_{\ell_1\ell_2}\sum_{\boldsymbol{\delta}_{\ell_1}\boldsymbol{\delta}_{\ell_2}}\sum_{\mathbf{k}_1}\sum_{\mathbf{q}}^{\mathrm{BZ}}\sum_{\mathbf{G}\mathbf{G}'}\psi^{\ell_1\ell_2}_{\mathbf{G}_1\mathbf{G}_2}(\mathbf{q})\times\\ \times\Big\{[M^{cc}_{\ell_1}(\mathbf{k},\mathbf{q},\mathbf{G}')]^*M^{cv}_{\ell_2}(\mathbf{k}_1,\mathbf{q},\mathbf{G})a^\dagger_{c,\mathbf{k}+\mathbf{q}}a^\dagger_{c\mathbf{k}_1}a_{v,\mathbf{k}_1+\mathbf{q}}a_{v\mathbf{k}}+\\ -[M^{vv}_{\ell_1}(\mathbf{k}-\mathbf{q},\mathbf{q},\mathbf{G}')]^*M^{cv}_{\ell_2}(\mathbf{k}_1,\mathbf{q},\mathbf{G})a^\dagger_{c\mathbf{k}}a^\dagger_{c\mathbf{k}_1}a_{v,\mathbf{k}_1+\mathbf{q}}a_{v,\mathbf{k}-\mathbf{q}}+\\ -[M^{cv}_{\ell_1}(\mathbf{k}_1,\mathbf{q},\mathbf{G}')]^*M^{cc}_{\ell_2}(\mathbf{k}-\mathbf{q},\mathbf{q},\mathbf{G})a^\dagger_{c,\mathbf{k}_1+\mathbf{q}}a^\dagger_{c,\mathbf{k}-\mathbf{q}}a_{v\mathbf{k}_1}a_{v\mathbf{k}}+\\ +[M^{cv}_{\ell_1}(\mathbf{k}_1,\mathbf{q},\mathbf{G}')]^*M^{vv}_{\ell_2}(\mathbf{k},\mathbf{q},\mathbf{G})a^\dagger_{c\mathbf{k}}a^\dagger_{c,\mathbf{k}_1+\mathbf{q}}a_{v,\mathbf{k}+\mathbf{q}}a_{v\mathbf{k}_1}\Big\}. \quad \text{(A.11)}\end{aligned}$$

Now that we calculated each commutator on the right-hand side of (A.2), we apply the expectation value $\langle . \rangle$ on both sides. The first two terms (A.4c) and (A.5c) are straightforward:

$$\langle[\mathcal{H}_0, a^\dagger_{c\mathbf{k}}a_{v\mathbf{k}}]\rangle = (E_{c\mathbf{k}} - E_{v\mathbf{k}})p_{cv}(\mathbf{k}), \quad \text{(A.12a)}$$

$$\langle[\mathcal{H}_I, a^\dagger_{c\mathbf{k}}a_{v\mathbf{k}}]\rangle = -\boldsymbol{\mathcal{E}}\cdot\mathbf{d}_{cv}(\mathbf{k}), \quad \text{(A.12b)}$$

where we defined the interband transition amplitude $p_{cv}(\mathbf{k}) = \langle a^\dagger_{c\mathbf{k}} a_{v\mathbf{k}} \rangle$ and noticed that

$$\langle a^\dagger_{v\mathbf{k}} a_{v\mathbf{k}} \rangle = \langle 0 | a^\dagger_{v\mathbf{k}} a_{v\mathbf{k}} | 0 \rangle = \langle 0 | 0 \rangle = 1, \tag{A.13a}$$

$$\langle a^\dagger_{c\mathbf{k}} a_{c\mathbf{k}} \rangle = \langle 0 | a^\dagger_{c\mathbf{k}} a_{c\mathbf{k}} | 0 \rangle = 0. \tag{A.13b}$$

The electron-electron interaction term (A.11) leads to an infinite hierarchy of n-body operators, $n = 2, 3, \ldots$. We will truncate it by applying the approximation

$$\langle a^\dagger_{n_1\mathbf{k}_1} a^\dagger_{n_2\mathbf{k}_2} a_{n_3\mathbf{k}_3} a_{n_4\mathbf{k}_4} \rangle \approx \langle a^\dagger_{n_1\mathbf{k}_1} a_{n_4\mathbf{k}_4} \rangle \langle a^\dagger_{n_2\mathbf{k}_2} a_{n_3\mathbf{k}_3} \rangle - \langle a^\dagger_{n_1\mathbf{k}_1} a_{n_3\mathbf{k}_3} \rangle \langle a^\dagger_{n_2\mathbf{k}_2} a_{n_4\mathbf{k}_4} \rangle, \tag{A.14}$$

which is justified under the RPA. Morever, since we are considering a homogeneous electric field, momentum is conserved in the electronic transitions. This is included through the relation

$$\langle a^\dagger_{c\mathbf{k}'} a_{v\mathbf{k}} \rangle = \delta_{\mathbf{k}\mathbf{k}'} p_{cv}(\mathbf{k}). \tag{A.15}$$

Thus,

$$\begin{aligned}
\langle [\mathcal{H}_{ee}, a^\dagger_{c\mathbf{k}} a_{v\mathbf{k}}] \rangle = -\frac{e}{2\mathcal{S}} \sum_{\ell_1\ell_2} \sum_{\mathbf{k}_1} \sum_{\mathbf{q}}^{\mathrm{BZ}} \sum_{\mathbf{G}\mathbf{G}'} \psi^{\ell_1\ell_2}_{\mathbf{G}\mathbf{G}'}(\mathbf{q}) \times \\
\times \Big\{ [M^{cc}_{\ell_1}(\mathbf{k}, \mathbf{q}, \mathbf{G}')]^* M^{cv}_{\ell_2}(\mathbf{k}_1, \mathbf{q}, \mathbf{G}) \left[p_{cv}(\mathbf{k}) p_{cv}(\mathbf{k}_1) \delta_{\mathbf{q}\mathbf{0}} - p^2_{cv}(\mathbf{k}) \delta_{\mathbf{k}\mathbf{k}_1} \right] + \\
- [M^{vv}_{\ell_1}(\mathbf{k}-\mathbf{q}, \mathbf{q}, \mathbf{G}')]^* M^{cv}_{\ell_2}(\mathbf{k}_1, \mathbf{q}, \mathbf{G}) \left[p_{cv}(\mathbf{k}) p_{cv}(\mathbf{k}_1) \delta_{\mathbf{q}\mathbf{0}} - p_{cv}(\mathbf{k}) p_{cv}(\mathbf{k}-\mathbf{q}) \delta_{\mathbf{k}_1,\mathbf{k}-\mathbf{q}} \right] + \\
- [M^{cv}_{\ell_1}(\mathbf{k}_1, \mathbf{q}, \mathbf{G}')]^* M^{cc}_{\ell_2}(\mathbf{k}-\mathbf{q}, \mathbf{q}, \mathbf{G}) \left[p_{cv}(\mathbf{k}) p_{cv}(\mathbf{k}-\mathbf{q}) \delta_{\mathbf{k}_1,\mathbf{k}-\mathbf{q}} - p_{cv}(\mathbf{k}_1) p_{cv}(\mathbf{k}) \delta_{\mathbf{q}\mathbf{0}} \right] + \\
+ [M^{cv}_{\ell_1}(\mathbf{k}_1, \mathbf{q}, \mathbf{G}')]^* M^{vv}_{\ell_2}(\mathbf{k}, \mathbf{q}, \mathbf{G}) \left[p_{cv}(\mathbf{k}) p_{cv}(\mathbf{k}+\mathbf{q}) \delta_{\mathbf{k}\mathbf{k}_1} - p_{cv}(\mathbf{k}) p_{cv}(\mathbf{k}_1) \delta_{\mathbf{q}\mathbf{0}} \right] \Big\}.
\end{aligned} \tag{A.16}$$

Contracting the delta functions with the correspondent summations, we have, after some rearrangement,

$$\begin{aligned}
\langle [\mathcal{H}_{ee}, a^\dagger_{c\mathbf{k}} a_{v\mathbf{k}}] \rangle = -\frac{e}{2\mathcal{S}} p_{cv}(\mathbf{k}) \sum_{\ell_1\ell_2} \sum_{\mathbf{G}\mathbf{G}'} \psi^{\ell_1\ell_2}_{\mathbf{G}\mathbf{G}'}(\mathbf{q}) \times \\
\times \Big\{ \sum_{\mathbf{k}_1} [M^{cc}_{\ell_1}(\mathbf{k}, \mathbf{0}, \mathbf{G}')]^* M^{cv}_{\ell_2}(\mathbf{k}_1, \mathbf{0}, \mathbf{G}) p_{cv}(\mathbf{k}_1) - [M^{vv}_{\ell_1}(\mathbf{k}, \mathbf{0}, \mathbf{G}')]^* M^{cv}_{\ell_2}(\mathbf{k}_1, \mathbf{0}, \mathbf{G}) p_{cv}(\mathbf{k}_1) + \\
+ [M^{cv}_{\ell_1}(\mathbf{k}_1, \mathbf{0}, \mathbf{G}')]^* M^{cc}_{\ell_2}(\mathbf{k}, \mathbf{0}, \mathbf{G}) p_{cv}(\mathbf{k}_1) - [M^{cv}_{\ell_1}(\mathbf{k}_1, \mathbf{0}, \mathbf{G}')]^* M^{vv}_{\ell_2}(\mathbf{k}, \mathbf{0}, \mathbf{G}) p_{cv}(\mathbf{k}_1) + \\
+ \sum_{\mathbf{q}}^{\mathrm{BZ}} - [M^{cc}_{\ell_1}(\mathbf{k}, \mathbf{q}, \mathbf{G}')]^* M^{cv}_{\ell_2}(\mathbf{k}, \mathbf{q}, \mathbf{G}) p_{cv}(\mathbf{k}) + [M^{vv}_{\ell_1}(\mathbf{k}-\mathbf{q}, \mathbf{q}, \mathbf{G}')]^* M^{cv}_{\ell_2}(\mathbf{k}-\mathbf{q}, \mathbf{q}, \mathbf{G}) p_{cv}(\mathbf{k}-\mathbf{q}) + \\
- [M^{cv}_{\ell_1}(\mathbf{k}-\mathbf{q}, \mathbf{q}, \mathbf{G}')]^* M^{cc}_{\ell_2}(\mathbf{k}-\mathbf{q}, \mathbf{q}, \mathbf{G}) p_{cv}(\mathbf{k}-\mathbf{q}) + [M^{cv}_{\ell_1}(\mathbf{k}, \mathbf{q}, \mathbf{G}')]^* M^{vv}_{\ell_2}(\mathbf{k}, \mathbf{q}, \mathbf{G}) p_{cv}(\mathbf{k}+\mathbf{q}) \Big\}.
\end{aligned} \tag{A.17}$$

Now we recognize an important property of the Bloch function overlap term

$$M_\ell^{nn'}(\mathbf{k},\mathbf{q},\mathbf{G})^* = M_\ell^{n'n}(\mathbf{k}+\mathbf{q},-\mathbf{q},-\mathbf{G}), \tag{A.18}$$

which allow us, after exchanging some summation indices, to simplify (A.17) to

$$\begin{aligned}\langle[\mathcal{H}_{ee}, a_{c\mathbf{k}}^\dagger a_{v\mathbf{k}}]\rangle = &-\frac{e}{\mathcal{S}} p_{cv}(\mathbf{k}) \sum_{\ell_1\ell_2}\sum_{\mathbf{G}\mathbf{G}'} \psi_{\mathbf{G}\mathbf{G}'}^{\ell_1\ell_2}(\mathbf{q})\times \\ \times \Bigg\{ &\sum_{\mathbf{k}'} [M_{\ell_1}^{cc}(\mathbf{k},\mathbf{0},\mathbf{G}')]^* M_{\ell_2}^{cv}(\mathbf{k}',\mathbf{0},\mathbf{G}) p_{cv}(\mathbf{k}') - [M_{\ell_1}^{vv}(\mathbf{k},\mathbf{0},\mathbf{G}')]^* M_{\ell_2}^{cv}(\mathbf{k}',\mathbf{0},\mathbf{G}) p_{cv}(\mathbf{k}') + \\ &+ \sum_{\mathbf{q}}^{\mathrm{BZ}} -[M_{\ell_1}^{cc}(\mathbf{k},\mathbf{q},\mathbf{G}')]^* M_{\ell_2}^{cv}(\mathbf{k},\mathbf{q},\mathbf{G}) p_{cv}(\mathbf{k}) + [M_{\ell_1}^{cv}(\mathbf{k},\mathbf{q},\mathbf{G}')]^* M_{\ell_2}^{vv}(\mathbf{k},\mathbf{q},\mathbf{G}) p_{cv}(\mathbf{k}) \Bigg\}.\end{aligned} \tag{A.19}$$

At this stage we must recognize the exchange self-energy

$$\begin{aligned}\Sigma_{\mathbf{k}} = &\frac{e}{\mathcal{S}} \sum_{\ell_1\ell_2}\sum_{\mathbf{G}\mathbf{G}'}\sum_{\mathbf{q}}^{\mathrm{BZ}} \psi_{\mathbf{G}\mathbf{G}'}^{\ell_1\ell_2}(\mathbf{q})\times \\ &\times \Big\{ [M_{\ell_1}^{cc}(\mathbf{k},\mathbf{q},\mathbf{G})]^* M_{\ell_2}^{cv}(\mathbf{k},\mathbf{q},\mathbf{G}) - [M_{\ell_1}^{cv}(\mathbf{k},\mathbf{q},\mathbf{G}')]^* M_{\ell_2}^{vv}(\mathbf{k},\mathbf{q},\mathbf{G}) \Big\},\end{aligned} \tag{A.20}$$

and the kernel

$$K(\mathbf{k},\mathbf{k}') = \sum_{\ell_1\ell_2}\sum_{\mathbf{G}\mathbf{G}'} \psi_{\mathbf{G}\mathbf{G}'}^{\ell_1\ell_2}(\mathbf{q}) \left[M_{\ell_1}^{cc}(\mathbf{k},\mathbf{0},\mathbf{G}') - M_{\ell_1}^{vv}(\mathbf{k},\mathbf{0},\mathbf{G}')\right]^* M_{\ell_2}^{cv}(\mathbf{k}',\mathbf{0},\mathbf{G}), \tag{A.21}$$

in order to rewrite (A.19) as

$$\langle[\mathcal{H}_{ee}, a_{c\mathbf{k}}^\dagger a_{v\mathbf{k}}]\rangle = p_{cv}(\mathbf{k}) \left[\Sigma_{\mathbf{k}} p_{cv}(\mathbf{k}) - \frac{e}{\mathcal{S}} \sum_{\mathbf{k}'} K(\mathbf{k},\mathbf{k}') p_{cv}(\mathbf{k}')\right]. \tag{A.22}$$

The final step is to gather Eqs. (A.1, A.12, A.22) and apply $\delta_t \to \mathrm{i}\omega$:

$$\hbar\omega p_{cv}(\mathbf{k}) = (E_{c\mathbf{k}} - E_{v\mathbf{k}}) p_{cv}(\mathbf{k}) - \boldsymbol{\mathcal{E}}\cdot\mathbf{d}_{cv}(\mathbf{k}) + \Sigma_{\mathbf{k}} p_{cv}(\mathbf{k}) - \frac{e}{\mathcal{S}}\sum_{\mathbf{k}'} K(\mathbf{k},\mathbf{k}') p_{cv}(\mathbf{k}'). \tag{A.23}$$

After some rearranging and recalling that, in our system of units, $e = 1$,

$$\hbar(\omega - \tilde{\omega}_{\mathbf{k}}) p_{cv}(\mathbf{k}) + \frac{1}{\mathcal{S}}\sum_{\mathbf{k}'} K(\mathbf{k},\mathbf{k}') p_{cv}(\mathbf{k}') = -\boldsymbol{\mathcal{E}}\cdot\mathbf{d}_{cv}(\mathbf{k}), \tag{A.24}$$

where we used the definition of the optical band $\hbar\tilde{\omega}_{\mathbf{k}} = E_{c\mathbf{k}} - E_{v\mathbf{k}} + \Sigma_{\mathbf{k}}$.

To obtain the dipole element, first we note that

$$\hat{\mathbf{r}}|\mathbf{R}+\boldsymbol{\delta}_\ell\rangle = (\mathbf{R}+\boldsymbol{\delta}_\ell)|\mathbf{R}+\boldsymbol{\delta}_\ell\rangle, \tag{A.25}$$

and so

$$\hat{\mathbf{r}}|n\mathbf{k}\rangle = \sum_{\mathbf{R},\boldsymbol{\delta}_\ell}(\mathbf{R}+\boldsymbol{\delta}_\ell)e^{i(\mathbf{R}+\boldsymbol{\delta}_\ell)\cdot\mathbf{k}}u_{n\boldsymbol{\delta}_\ell}(\mathbf{k})|\mathbf{R}+\boldsymbol{\delta}_\ell\rangle. \tag{A.26}$$

Defining

$$\hat{H}_\mathbf{k} = \sum_n E_{n\mathbf{k}}|n\mathbf{k}\rangle\langle n\mathbf{k}|, \tag{A.27}$$

we have

$$[\hat{H}_\mathbf{k},\hat{\mathbf{r}}] = \sum_n E_{n\mathbf{k}}\sum_{\mathbf{R},\boldsymbol{\delta}_\ell}[(\mathbf{R}+\boldsymbol{\delta}_\ell)-(\mathbf{R}'+\boldsymbol{\delta}'_\ell)]\times \\ \times e^{i(\mathbf{R}+\boldsymbol{\delta}_\ell)\cdot\mathbf{k}}u_{n\boldsymbol{\delta}_\ell}(\mathbf{k})e^{-i(\mathbf{R}'+\boldsymbol{\delta}'_\ell)\cdot\mathbf{k}}u^*_{n\boldsymbol{\delta}_{\ell'}}(\mathbf{k})|\mathbf{R}+\boldsymbol{\delta}_\ell\rangle\langle\mathbf{R}'+\boldsymbol{\delta}'_{\ell'}|, \tag{A.28}$$

that can be rewritten as

$$[\hat{H}_\mathbf{k},\hat{\mathbf{r}}] = \nabla_\mathbf{k}\hat{H}_\mathbf{k} - \sum_n\Bigg[\nabla_\mathbf{k}\left(E_{n\mathbf{k}}\right)|\mathbf{k}n\rangle\langle\mathbf{k}n| - \sum_{\mathbf{R},\boldsymbol{\delta}_\ell}\sum_{\mathbf{R}',\boldsymbol{\delta}'_\ell}\nabla_\mathbf{k}\left(u^*_{n\boldsymbol{\delta}_{\ell'}}(\mathbf{k})u_{n\boldsymbol{\delta}_\ell}(\mathbf{k})\right)\times \\ \times e^{-i(\mathbf{R}'+\boldsymbol{\delta}'_\ell)\cdot\mathbf{k}}e^{i(\mathbf{R}+\boldsymbol{\delta}_\ell)\cdot\mathbf{k}}|\mathbf{R}+\boldsymbol{\delta}_\ell\rangle\langle\mathbf{R}'+\boldsymbol{\delta}'_{\ell'}|. \tag{A.29}$$

Now for $m\neq n$,

$$\langle m\mathbf{k}|[\hat{H}_\mathbf{k},\hat{\mathbf{r}}]|n\mathbf{k}\rangle = \langle m\mathbf{k}|\nabla_\mathbf{k}\hat{H}_\mathbf{k}|n\mathbf{k}\rangle + \\ -\sum_{n'}\sum_{\mathbf{R},\boldsymbol{\delta}_\ell}\sum_{\mathbf{R}',\boldsymbol{\delta}'_\ell}\nabla_\mathbf{k}\left(u^*_{n'\boldsymbol{\delta}_{\ell'}}(\mathbf{k})u_{n'\boldsymbol{\delta}_\ell}(\mathbf{k})\right)u^*_{m\boldsymbol{\delta}_\ell}(\mathbf{k})u_{n\boldsymbol{\delta}'_\ell}, \tag{A.30}$$

and we can show that

$$\sum_{n'}\sum_{\mathbf{R},\boldsymbol{\delta}_\ell}\sum_{\mathbf{R}',\boldsymbol{\delta}'_\ell}\nabla_\mathbf{k}\left(u^*_{n'\boldsymbol{\delta}_{\ell'}}(\mathbf{k})u_{n'\boldsymbol{\delta}_\ell}(\mathbf{k})\right)u^*_{m\boldsymbol{\delta}_\ell}(\mathbf{k})u_{n\boldsymbol{\delta}'_\ell} = 0. \tag{A.31}$$

Thus,

$$\langle m\mathbf{k}|[\hat{H}_\mathbf{k},\hat{\mathbf{r}}]|n\mathbf{k}\rangle = i\langle m\mathbf{k}|\nabla_\mathbf{k}\hat{H}_\mathbf{k}|n\mathbf{k}\rangle, \tag{A.32}$$

and using that

$$\langle n\mathbf{k}|[\hat{H},\hat{\mathbf{r}}]|m\mathbf{k}\rangle = (E_{n,\mathbf{k}}-E_{m,\mathbf{k}})\langle n\mathbf{k}|\hat{\mathbf{r}}|m\mathbf{k}\rangle, \tag{A.33}$$

finally

$$\mathbf{d}_{cv}(\mathbf{k}) = \frac{\langle c,\mathbf{k}|\nabla_\mathbf{k}\hat{H}_\mathbf{k}|\mathbf{k},v\rangle}{E_{c,\mathbf{k}}-E_{v,\mathbf{k}}}. \tag{A.34}$$

Appendix B - Presentations at conferences

Partial results of this work have been presented as posters or oral presentations in national and international conferences. They are listed below.

1. DUARTE, V. G. M.; CALEIRO, L. T.; CHAVES, A. J.; GUILHON, I.; MARQUES, M.; GOMES, T. C. F.; TELES, L. K. A simplified tight-binding approach to the investigation of electronic structures in twisted bilayer graphene and transitional metal dichalcogenides. Encontro de Outono 2022, Apr. 10-14, 2022 - São Paulo, SP, Brazil. Poster presentation.

2. DUARTE, V. G. M.; CALEIRO, L. T.; CHAVES, A. J.; DA COSTA, D.R.; GUILHON, I.; MARQUES, M.; GOMES, T. C. F.; TELES, L. K. An efficient tight-binding approach for the investigation of twisted bilayers of graphene and molybdenum disulfide near the magic angle. Frontiers in Quantum Materials and Devices 2020, Jun. 20-24, 2022 - Valencia, Spain. Poster presentation.

3. DUARTE, V. G. M.; CALEIRO, L. T.; CHAVES, A. J.; DA COSTA, D.R.; GUILHON, I.; MARQUES, M.; GOMES, T. C. F.; TELES, L. K. An efficient tight-binding approach for the investigation of twisted bilayers of graphene and molybdenum disulfide near the magic angle. XV Encontro de Física do ITA, Jul. 4-8, 2022 - São José dos Campos, SP, Brazil. Poster presentation.

4. DUARTE, V. G. M.; CHAVES, A. J.; DA COSTA, D. R.; GUILHON, I.; MARQUES, M.; TELES, L. K. Efficient and extensible tight-binding model for twisted bilayer graphene. Brazilian Workshop on Semiconductor Physics (BWSP-2022), Sep. 12-16, 2022 - São José dos Campos, SP, Brazil. Poster and oral presentation.

5. DUARTE, V. G. M.; DA COSTA, D. R.; PERES, N. M. R.; TELES, L. K.; CHAVES, A. J. Excitons in biased twisted bilayer graphene under pressure. Encontro de Outono 2023, May 21-25, 2023 - Ouro Preto, MG, Brazil. Oral presentation.

6. DUARTE, V. G. M.; DA COSTA, D. R.; PERES, N. M. R.; TELES, L. K.; CHAVES, A. J. Excitons in biased twisted bilayer graphene under pressure. School on Emergent

Phenomena in Non-Equilibrium Quantum Many-Body Systems, June 26 - July 7, 2023 - São Paulo, SP, Brazil. Oral presentation.

FOLHA DE REGISTRO DO DOCUMENTO

1. CLASSIFICAÇÃO/TIPO	2. DATA	3. REGISTRO N°	4. N° DE PÁGINAS
DM	16 de agosto de 2023	DCTA/ITA/DM-072/2023	68

5. TÍTULO E SUBTÍTULO:

Electronic properties of twisted bilayer graphene: pressure and electrostatic bias dependence

6. AUTOR(ES):

Victor Gabriel Morele Duarte

7. INSTITUIÇÃO(ÕES)/ÓRGÃO(S) INTERNO(S)/DIVISÃO(ÕES):

Instituto Tecnológico de Aeronáutica - ITA

8. PALAVRAS-CHAVE SUGERIDAS PELO AUTOR:

Graphene; Twistronics; Tight-binding; Excitons; Two-dimensional materials; Photonics.

9.PALAVRAS-CHAVE RESULTANTES DE INDEXAÇÃO:

Grafeno; Estruturas bidimensionais; Semicondutores; Propriedades ópticas; Dispositivos optoeletrônicos; Fotônica; Óptica; Física.

10. APRESENTAÇÃO: **(X) Nacional ( ) Internacional**

ITA, São José dos Campos. Curso de Mestrado. Programa de Pós-Graduação em Física. Área de Física Atômica. Orientador: Prof. Dr. André Jorge Carvalho Chaves; coorientadora: Profa. Dra. Lara Kuhl Teles. Defesa em 25/07/2023. Publicada em 2023.

11. RESUMO:

This study investigates light-matter interactions in layered 2D materials with prominent band gaps, focusing on the formation of excitons. The specific system under examination consists of two layers of graphene with a twist, a well-documented configuration in the literature known for its manifestation of various exotic phenomena. Unlike AB bilayer graphene, this system does not naturally exhibit a band gap under typical conditions, in contrast to the application of an applied bias. Using a tight-binding model, we theoretically demonstrated that Twisted Bilayer Graphene (TBG) can be modulated through vertical bias and pressure to function as a narrow band gap semiconductor, capable of hosting a spectrum of anisotropic bound excitons highly hybridized between the graphene layers. The gap opens under high pressure and can be further enhanced by an electric bias, with values reaching up to 200 meV. In terms of the band structure, the band gap is located between the M and K points of the superlattice Brillouin Zone. Utilizing the Semiconductor Bloch Equations (SBE) formalism, we analyze the impact of electron-electron interactions and observe an enhancement of the band gap. By solving the homogeneous SBE, we demonstrate the presence of highly anisotropic excitons with strong electron-hole hybridization between different layers. The optical spectra of the system, which we calculated by solving the complete SBE, exhibit a diverse range of absorption peaks, which indicate that the excitons of TBG can be detected experimentally by optical signatures.

12. GRAU DE SIGILO:

(X) OSTENSIVO ( ) RESERVADO ( ) SECRETO